

# Comprehensive evaluations of diurnal NO<sub>2</sub> measurements during DISCOVER-AQ 2011: Effects of resolution dependent representation of NO<sub>x</sub> emissions

Jianfeng Li<sup>1, a</sup>, Yuhang Wang<sup>1\*</sup>, Ruixiong Zhang<sup>1</sup>, Charles Smeltzer<sup>1</sup>, Andrew Weinheimer<sup>2</sup>, Jay Herman<sup>3</sup>, K.  
Folkert Boersma<sup>4, 5</sup>, Edward A. Celarier<sup>6, 7, b</sup>, Russell W. Long<sup>8</sup>, James J. Szykman<sup>8</sup>, Ruben Delgado<sup>3</sup>, Anne M.  
Thompson<sup>6</sup>, Travis N. Knepp<sup>9, 10</sup>, Lok N. Lamsal<sup>6</sup>, Scott J. Janz<sup>6</sup>, Matthew G. Kowalewski<sup>6</sup>, Xiong Liu<sup>11</sup>,  
Caroline R. Nowlan<sup>11</sup>

<sup>1</sup>School of Earth and Atmospheric Sciences, Georgia Institute of Technology, Atlanta, Georgia, USA

<sup>2</sup>National Center for Atmospheric Research, Boulder, Colorado, USA

<sup>3</sup>University of Maryland Baltimore County JCET, Baltimore, Maryland, USA

<sup>4</sup>Royal Netherlands Meteorological Institute, De Bilt, the Netherlands

<sup>5</sup>Wageningen University, Meteorology and Air Quality Group, Wageningen, the Netherlands

<sup>6</sup>NASA Goddard Space Flight Center, Greenbelt, Maryland, USA

<sup>7</sup>Universities Space Research Association, Columbia, Maryland, USA

<sup>8</sup>National Exposure Research Laboratory, Office of Research and Development, U.S. Environmental Protection  
Agency, Research Triangle Park, NC, USA

<sup>9</sup>NASA Langley Research Center, Virginia, USA

<sup>10</sup>Science Systems and Applications, Inc., Hampton, Virginia, USA

<sup>11</sup>Harvard-Smithsonian Center for Astrophysics, Cambridge, Massachusetts, USA

<sup>a</sup>now at: Atmospheric Sciences and Global Change Division, Pacific Northwest National Laboratory, Richland,  
Washington, USA

<sup>b</sup>now at: Digital Spec, Tyson's Corner, VA, USA

\* Correspondence to Yuhang Wang (yuhang.wang@eas.gatech.edu)

## 26    **Abstract**

27    Nitrogen oxides ( $\text{NO}_x = \text{NO} + \text{NO}_2$ ) play a crucial role in the formation of ozone and secondary inorganic and  
28    organic aerosols, thus affecting human health, global radiation budget, and climate. The diurnal and spatial  
29    variations of  $\text{NO}_2$  are functions of emissions, advection, deposition, vertical mixing, and chemistry. Their  
30    observations, therefore, provide useful constraints in our understanding of these factors. We employ a Regional  
31    chEmical and trAnsport model (REAM) to analyze the observed temporal (diurnal cycles) and spatial  
32    distributions of  $\text{NO}_2$  concentrations and tropospheric vertical column densities (TVCDs) using aircraft in situ  
33    measurements, surface EPA Air Quality System (AQS) observations, as well as the measurements of TVCDs by  
34    satellite instruments (OMI: the Ozone Monitoring Instrument; and GOME-2A: Global Ozone Monitoring  
35    Experiment – 2A), ground-based Pandora, and the Airborne Compact Atmospheric Mapper (ACAM) instrument,  
36    in July 2011 during the DISCOVER-AQ campaign over the Baltimore-Washington region. The model  
37    simulations at 36- and 4-km resolutions are in reasonably good agreement with the regional mean temporospatial  
38     $\text{NO}_2$  observations in the daytime. However, nighttime mixing in the model needs to be enhanced to reproduce the  
39    observed  $\text{NO}_2$  diurnal cycle in the model. Another discrepancy is that Pandora measured  $\text{NO}_2$  TVCDs show much  
40    less variation in the late afternoon than simulated in the model. The higher resolution 4-km simulations tend to  
41    show larger biases compared to the observations due largely to the larger spatial variations of  $\text{NO}_x$  emissions in  
42    the model when the model spatial resolution is increased from 36 to 4 km. OMI, GOME-2A, and the high-  
43    resolution aircraft ACAM observations show a more dispersed distribution of  $\text{NO}_2$  vertical column densities  
44    (VCDs) and lower VCDs in urban regions than corresponding 36- and 4-km model simulations, reflecting likely  
45    the spatial distribution bias of  $\text{NO}_x$  emissions in the National Emissions Inventory (NEI) 2011.

# 46 1 Introduction

47 Nitrogen oxides ( $\text{NO}_x = \text{NO} + \text{NO}_2$ ) are among the most important trace gases in the atmosphere due to their  
48 crucial role in the formation of ozone ( $\text{O}_3$ ), secondary aerosols, and their role in the chemical transformation of  
49 other atmospheric species, such as carbon monoxide ( $\text{CO}$ ) and volatile organic compounds (VOCs) (Cheng et al.,  
50 2017; Cheng et al., 2018; Fisher et al., 2016; Li et al., 2019; Liu et al., 2012; Ng et al., 2017; Peng et al., 2016;  
51 Zhang and Wang, 2016).  $\text{NO}_x$  is emitted by both anthropogenic activities and natural sources. Anthropogenic  
52 sources account for about 77% of the global  $\text{NO}_x$  emissions, and fossil fuel combustion and industrial processes  
53 are the primary anthropogenic sources, which contribute to about 75% of the anthropogenic emissions (Seinfeld  
54 and Pandis, 2016). Other important anthropogenic sources include agriculture and biomass and biofuel burning.  
55 Soils and lightning are two major natural sources. Most  $\text{NO}_x$  is emitted as  $\text{NO}$ , which is then oxidized to  $\text{NO}_2$  by  
56 oxidants, such as  $\text{O}_3$ , the hydroperoxyl radical ( $\text{HO}_2$ ), and organic peroxy radicals ( $\text{RO}_2$ ).

57 The diurnal variations of  $\text{NO}_2$  controlled by physical and chemical processes reflect the temporal patterns of  
58 these underlying controlling factors, such as  $\text{NO}_x$  emissions, chemistry, deposition, advection, diffusion, and  
59 convection. Therefore, the observations of  $\text{NO}_2$  diurnal cycles can be used to evaluate our understanding of  $\text{NO}_x$   
60 related emission, chemistry, and physical processes (Frey et al., 2013; Jones et al., 2000; Judd et al., 2018). For  
61 example, Brown et al. (2004) analyzed the diurnal patterns of surface  $\text{NO}$ ,  $\text{NO}_2$ ,  $\text{NO}_3$ ,  $\text{N}_2\text{O}_5$ ,  $\text{HNO}_3$ ,  $\text{OH}$ , and  $\text{O}_3$   
62 concentrations along the East Coast of the United States (U.S.) during the New England Air Quality Study  
63 (NEAQS) campaign in the summer of 2002 and found that the predominant nighttime sink of  $\text{NO}_x$  through the  
64 hydrolysis of  $\text{N}_2\text{O}_5$  had an efficiency on par with daytime photochemical loss over the ocean surface off the New  
65 England coast. Van Stratum et al. (2012) investigated the contribution of boundary layer dynamics to chemistry  
66 evolution during the DOMINO (Diel Oxidant Mechanisms in relation to Nitrogen Oxides) campaign in 2008 in  
67 Spain and found that entrainment and boundary layer growth in daytime influenced mixed-layer  $\text{NO}$  and  $\text{NO}_2$

68 diurnal cycles on the same order of chemical transformations. David and Nair (2011) found that the diurnal  
69 patterns of surface NO, NO<sub>2</sub>, and O<sub>3</sub> concentrations at a tropical coastal station in India from November 2007 to  
70 May 2009 were closely associated with sea breeze and land breeze which affected the availability of NO<sub>x</sub> through  
71 transport. They also thought that monsoon-associated synoptic wind patterns could strongly influence the  
72 magnitudes of NO, NO<sub>2</sub>, and O<sub>3</sub> diurnal cycles. The monsoon effect on surface NO, NO<sub>2</sub>, and O<sub>3</sub> diurnal cycles  
73 was also observed in China by Tu et al. (2007) on the basis of continuous measurements of NO, NO<sub>2</sub>, and O<sub>3</sub> at  
74 an urban site in Nanjing from January 2000 – February 2003.

75 In addition to surface NO<sub>2</sub> diurnal cycles, the daily variations of NO<sub>2</sub> vertical column densities (VCDs) were  
76 also investigated in previous studies. For example, Boersma et al. (2008) compared NO<sub>2</sub> tropospheric VCDs  
77 (TVCDs) retrieved from OMI (the Ozone Monitoring Instrument) and SCIAMACHY (SCanning Imaging  
78 Absorption SpectroMeter for Atmospheric CHartography) in August 2006 around the world. They found that the  
79 diurnal patterns of different types of NO<sub>x</sub> emissions could strongly affect the NO<sub>2</sub> TVCD variations between  
80 OMI and SCIAMACHY and that intense afternoon fire activity resulted in an increase of NO<sub>2</sub> TVCDs from  
81 10:00 LT (local time) to 13:30 LT over tropical biomass burning regions. Boersma et al. (2009) further  
82 investigated the NO<sub>2</sub> TVCD change from SCIAMACHY to OMI in different seasons of 2006 in Israeli cities and  
83 found that there was a slight increase of NO<sub>2</sub> TVCDs from SCIAMACHY to OMI in winter due to increased NO<sub>x</sub>  
84 emissions from 10:00 LT to 13:30 LT and a sufficiently weak photochemical sink and that the TVCDs from OMI  
85 were lower than SCIAMACHY in summer due to a strong photochemical sink of NO<sub>x</sub>.

86 All these above researches, however, exploited only NO<sub>2</sub> surface or satellite VCD measurements. Due to the  
87 availability of ground-based NO<sub>2</sub> VCD observations, some recent studies tried to investigate the diurnal  
88 relationships between NO<sub>2</sub> surface concentrations and NO<sub>2</sub> VCDs (Kollonige et al., 2018; Thompson et al.,  
89 2019). For example, Zhao et al. (2019) converted Pandora direct-sun and zenith-sky NO<sub>2</sub> VCDs to NO<sub>2</sub> surface

90 concentrations using concentration-to-partial-column ratios and found that the derived concentrations well  
91 captured the observed NO<sub>2</sub> surface diurnal and seasonal variations. Knepp et al. (2015) related the daytime  
92 variations of NO<sub>2</sub> TVCD measurements by ground-based Pandora instruments to the variations of coincident NO<sub>2</sub>  
93 surface concentrations using a planetary boundary layer height (PBLH) factor over the periods July 2011 –  
94 October 2011 at the NASA Langley Research Center in Hampton, Virginia and July 2011 at Padonia and  
95 Edgewood sites in Maryland for the DISCOVER-AQ experiment, showing the importance of boundary-layer  
96 vertical mixing on NO<sub>2</sub> vertical distributions and the ability of NO<sub>2</sub> VCD measurements to infer hourly  
97 boundary-layer NO<sub>2</sub> variations. DISCOVER-AQ, the Deriving Information on Surface conditions from Column  
98 and Vertically Resolved Observations Relevant to Air Quality experiment (<https://discover-aq.larc.nasa.gov/>, last  
99 access: April 6, 2019), was designed to better understand the relationship between boundary-layer pollutants and  
100 satellite observations (Flynn et al., 2014; Reed et al., 2015). Figure 1 shows the sampling locations of the summer  
101 DISCOVER-AQ 2011 campaign in the Baltimore-Washington metropolitan region. In this campaign, the NASA  
102 P-3B aircraft flew spirals over six air quality monitoring sites (Aldino - rural/suburban, Edgewood -  
103 coastal/urban, Beltsville - suburban, Essex - coastal/urban, Fairhill - rural, and Padonia - suburban) (Table S1)  
104 and the Chesapeake Bay (Cheng et al., 2017; Lamsal et al., 2014), and measured 245 NO<sub>2</sub> profiles in 14 flight  
105 days in July (Zhang et al., 2016). During the same period, the NASA UC-12 aircraft flew across the Baltimore-  
106 Washington region at an altitude about 8 km above sea level (ASL), using the Airborne Compact Atmospheric  
107 Mapper (ACAM) to map the distributions of NO<sub>2</sub> VCDs below the aircraft (Lamsal et al., 2017). Furthermore,  
108 ground-based instruments were deployed to measure NO<sub>2</sub> surface concentrations, NO<sub>2</sub> VCDs, and other physical  
109 properties of the atmosphere (Anderson et al., 2014; Reed et al., 2015; Sawamura et al., 2014). Satellite OMI and  
110 GOME-2A (Global Ozone Monitoring Experiment – 2A) instruments provided NO<sub>2</sub> TVCD measurements over  
111 the campaign region at 13:30 and 9:30 LT, respectively. These concurrent measurements of NO<sub>2</sub> VCDs, surface  
112 NO<sub>2</sub>, and vertically resolved distributions of NO<sub>2</sub> during the DISCOVER-AQ 2011 campaign, therefore, provide

113 a comprehensive dataset to evaluate NO<sub>2</sub> diurnal and spatial variabilities and processes affecting NO<sub>2</sub>  
114 concentrations.

115 Section 2 describes the measurement datasets in detail. The Regional chEmistry and trAnsport Model  
116 (REAM), also described in section 2, is applied to simulate the NO<sub>2</sub> observations during the DISCOVER-AQ  
117 campaign in July 2011. The evaluations of the simulated diurnal cycles of surface NO<sub>2</sub> concentrations, NO<sub>2</sub>  
118 vertical profiles, and NO<sub>2</sub> TVCDs are discussed in section 3 through comparisons with observations. In section 3,  
119 we also investigate the differences between NO<sub>2</sub> diurnal cycles on weekdays and weekends and their implications  
120 for NO<sub>x</sub> emission characteristics. To corroborate our evaluation of NO<sub>x</sub> emissions based on NO<sub>2</sub> diurnal cycles,  
121 we further compare observed NO<sub>y</sub> (reactive nitrogen compounds) concentrations with REAM simulation results  
122 in section 3. Moreover, we assess the resolution dependence of REAM simulation results in light of the  
123 observations and discuss the potential distribution biases of NO<sub>x</sub> emissions by comparing the 36- and 4-km  
124 REAM simulation results with OMI, GOME-2A, and high-resolution ACAM NO<sub>2</sub> VCDs. Finally, we summarize  
125 the study in section 4.

## 126 **2 Datasets and model description**

### 127 **2.1 REAM**

128 REAM has been widely applied in many studies (Cheng et al., 2017; Choi et al., 2008; Li et al., 2019; Zhang  
129 et al., 2018; Zhang et al., 2016; Zhao et al., 2009). The model has a horizontal resolution of 36 km and 30 vertical  
130 layers in the troposphere. Meteorology fields are from a Weather Research and Forecasting (WRF, version 3.6)  
131 model simulation with a horizontal resolution of 36 km. We summarize the physics parameterization schemes of  
132 the WRF simulation in Table S2. The WRF simulation is initialized and constrained by the NCEP coupled  
133 forecast system model version 2 (CFSv2) products (<http://rda.ucar.edu/datasets/ds094.0/>, last access: March 10,

2015) (Saha et al., 2011). The chemistry mechanism in REAM is based on GEOS-Chem v11.01 with updated aerosol uptake of isoprene nitrates (Fisher et al., 2016) and revised treatment of wet scavenging processes (Luo et al., 2019). A  $2^\circ \times 2.5^\circ$  GEOS-Chem simulation provides the chemical boundary and initial conditions.

Biogenic VOC emissions in REAM are from MEGAN v2.10 (Guenther et al., 2012). Anthropogenic emissions on weekdays are from the National Emission Inventory 2011 (NEI2011) (EPA, 2014) from the Pacific Northwest National Laboratory (PNNL), which has an initial resolution of 4 km and is re-gridded to REAM 36-km grid cells (Figure 2). Weekday emission diurnal profiles are from NEI2011. The weekday to weekend emission ratios and weekend emission diurnal profiles are based on previous studies (Beirle et al., 2003; Boersma et al., 2009; Choi et al., 2012; de Foy, 2018; DenBleyker et al., 2012; Herman et al., 2009; Judd et al., 2018; Kaynak et al., 2009; Kim et al., 2016). These studies suggested that weekend  $\text{NO}_x$  emissions were 20% - 50% lower than weekday emissions, and the weekend  $\text{NO}_x$  emission diurnal cycles were different from weekdays; therefore, we specify a weekend to weekday  $\text{NO}_x$  emission ratio of 2/3 in this study. The resulting diurnal variations of weekday and weekend  $\text{NO}_x$  emissions over the DISCOVER-AQ 2011 region are shown in Figure 3. The diurnal emission variation is lower on weekends than on weekdays.

To understand the effects of model resolutions on the temporospatial distributions of  $\text{NO}_2$ , we also conduct a REAM simulation with a horizontal resolution of 4 km during the DISCOVER-AQ campaign. A 36-km REAM simulation (discussed in section 3.2) provides the chemical initial and hourly boundary conditions. Meteorology fields are from a nested WRF simulation (36 km, 12 km, 4 km) with cumulus parameterization turned off in the 4-km domain (Table S2). Figure 1 shows a comparison of the 4-km and 36-km REAM grid cells with DISCOVER-AQ observations, and Figure 2 shows a comparison of  $\text{NO}_x$  emission distributions between the 4-km and 36-km REAM simulations. The comparison of  $\text{NO}_x$  emission diurnal variations over the DISCOVER-AQ 2011 region between the 4-km and 36-km REAM is shown in Figure 3.

## 2.2 NO<sub>2</sub> TVCD measurements by OMI and GOME-2A

The OMI instrument onboard the sun-synchronous NASA EOS Aura satellite with an equator-crossing time of around 13:30 LT was developed by the Finnish Meteorological Institute and the Netherlands Agency for Aerospace Programs to measure solar backscattering radiation in the visible and ultraviolet bands (Levelt et al., 2006; Russell et al., 2012). The radiance measurements are used to derive trace gas concentrations in the atmosphere, such as O<sub>3</sub>, NO<sub>2</sub>, HCHO, and SO<sub>2</sub> (Levelt et al., 2006). OMI has a nadir resolution of 13 km × 24 km and provides daily global coverage (Levelt et al., 2006).

Two widely-used archives of OMI NO<sub>2</sub> VCD products are available, NASA OMNO2 (v4.0) ([https://disc.gsfc.nasa.gov/datasets/OMNO2\\_003/summary](https://disc.gsfc.nasa.gov/datasets/OMNO2_003/summary), last access: September 26, 2020) and KNMI DOMINO (v2.0) (<http://www.temis.nl/airpollution/no2.html>, last access: January 14, 2015). Although both use Differential Optical Absorption Spectroscopy (DOAS) algorithms to derive NO<sub>2</sub> slant column densities, they have differences in spectral fitting, stratospheric and tropospheric NO<sub>2</sub> slant column density (SCD) separation, a priori NO<sub>2</sub> vertical profiles, and air mass factor (AMF) calculation, etc. (Boersma et al., 2011; Bucsela et al., 2013; Chance, 2002; Krotkov et al., 2017; Lamsal et al., 2020; Marchenko et al., 2015; Oetjen et al., 2013; van der A et al., 2010; Van Geffen et al., 2015). Both OMNO2 and DOMINO have been extensively evaluated with field measurements and models (Boersma et al., 2009; Boersma et al., 2011; Choi et al., 2020; Hains et al., 2010; Huijnen et al., 2010; Ionov et al., 2008; Irie et al., 2008; Lamsal et al., 2014; Lamsal et al., 2020; Oetjen et al., 2013). The estimated uncertainty of DOMINO TVCD product includes an absolute component of  $1.0 \times 10^{15}$  molecules cm<sup>-2</sup> and a relative AMF component of 25% (Boersma et al., 2011), while the uncertainty of OMNO2 TVCD product ranges from ~30% under clear-sky conditions to ~60% under cloudy conditions (Lamsal et al., 2014; Oetjen et al., 2013; Tong et al., 2015). In order to reduce uncertainties in this study, we only use TVCD data with effective cloud fractions < 0.2, solar zenith angle (SZA) < 80°, and albedo ≤ 0.3. Both positive and



negative TVCDs are considered in the calculation. The data affected by row anomaly are excluded (Boersma et al., 2018; Zhang et al., 2018).

For AMF calculation, DOMINO used daily TM4 model results with a resolution of  $3^{\circ} \times 2^{\circ}$  as a priori  $\text{NO}_2$  vertical profiles (Boersma et al., 2007; Boersma et al., 2011), while OMNO2 v4.0 used monthly mean values from the Global Modeling Initiative (GMI) model with a resolution of  $1^{\circ} \times 1.25^{\circ}$ . The relatively coarse horizontal resolution of the a priori  $\text{NO}_2$  profiles in the retrievals can introduce uncertainties in the spatial and temporal characteristics of  $\text{NO}_2$  TVCDs at satellite pixel scales. For comparison purposes, we also use 36-km REAM simulation results as the a priori  $\text{NO}_2$  profiles to compute the AMFs and  $\text{NO}_2$  TVCDs with the DOMINO algorithm. The 36-km REAM  $\text{NO}_2$  data are first regridded to OMI pixels to calculate the corresponding tropospheric AMFs, which are then applied to compute OMI  $\text{NO}_2$  TVCDs by dividing the tropospheric SCDs from the DOMINO product by our updated AMFs.

The GOME-2 instrument onboard the polar-orbiting MetOp-A satellite (now referred to as GOME-2A) is an improved version of GOME-1 launched in 1995 and has an overpass time of 9:30 LT and a spatial resolution of  $80 \times 40 \text{ km}^2$  (Munro et al., 2006; Peters et al., 2012). GOME-2A measures backscattered solar radiation in the range from 240 nm to 790 nm, which is used for VCD retrievals of trace gases, such as  $\text{O}_3$ ,  $\text{NO}_2$ , BrO, and  $\text{SO}_2$  (Munro et al., 2006). We use the KNMI TM4NO2A v2.3 GOME-2A  $\text{NO}_2$  VCD product archived on [http://www.temis.nl/airpollution/no2col/no2colgome2\\_v2.php](http://www.temis.nl/airpollution/no2col/no2colgome2_v2.php) (last access: January 22, 2015) (Boersma et al., 2007; Boersma et al., 2011). GOME-2A derived  $\text{NO}_2$  VCDs have been validated with SCIAMACHY and MAX-DOAS measurements (Irie et al., 2012; Peters et al., 2012; Richter et al., 2011). As in the case of OMI, we use the same criteria to filter the  $\text{NO}_2$  TVCD data and recalculate the tropospheric AMF values and GOME-2A TVCDs using the daily 36-km REAM  $\text{NO}_2$  profiles (9:00 LT – 10:00 LT).

## 199 2.3 Pandora ground-based NO<sub>2</sub> VCD measurements

200 Pandora is a small direct sun spectrometer, which measures sun and sky radiance from 270 to 530 nm with a  
201 0.5 nm resolution and a 1.6° field of view (FOV) for the retrieval of the total VCDs of NO<sub>2</sub> with a precision of  
202 about  $5.4 \times 10^{14}$  molecules/cm<sup>2</sup> ( $2.7 \times 10^{14}$  molecules/cm<sup>2</sup> for NO<sub>2</sub> SCD) and a nominal accuracy of  $2.7 \times 10^{15}$   
203 molecules cm<sup>-2</sup> under clear-sky conditions (Herman et al., 2009; Lamsal et al., 2014; Zhao et al., 2020). There  
204 were 12 Pandora sites operating in the DISCOVER-AQ campaign (Figure 1). Six of them are the same as the P-  
205 3B aircraft spiral locations (Aldino, Edgewood, Beltsville, Essex, Fairhill, and Padonia) (Table S1 and Figure 1).  
206 The other six sites are Naval Academy (Annapolis Maryland) (USNA – ocean), University of Maryland College  
207 Park (UMCP – urban), University of Maryland Baltimore County (UMBC – urban), Smithsonian Environmental  
208 Research Center (SERC – rural/coastal), Oldtown in Baltimore (Oldtown – urban), and Goddard Space Flight  
209 Center (GSFC – urban/suburban) (Table S1 and Figure 1). In this study, we exclude the USNA site as its  
210 measurements were conducted on a ship (“Pandora(w)” in Figure 1), and there were no other surface  
211 observations in the corresponding REAM grid cell. Including the data from the USNA site has a negligible effect  
212 on the comparisons of observed and simulated NO<sub>2</sub> TVCDs. In our analysis, we ignore Pandora measurements  
213 with SZA > 80° (Figure S1) and exclude the data when fewer than three valid measurements are available within  
214 an hour to reduce the uncertainties of the hourly averages due to the significant variations of Pandora  
215 observations (Figure S2).

216 Since Pandora measures total NO<sub>2</sub> VCDs, we need to subtract stratosphere NO<sub>2</sub> VCDs from the total VCDs  
217 to compute TVCDs. As shown in Figure S3, stratosphere NO<sub>2</sub> VCDs show a clear diurnal cycle with an increase  
218 during daytime due in part to the photolysis of reactive nitrogen reservoirs such as N<sub>2</sub>O<sub>5</sub> and HNO<sub>3</sub> (Brohede et  
219 al., 2007; Dirksen et al., 2011; Peters et al., 2012; Sen et al., 1998; Spinei et al., 2014), which is consistent with  
220 the significant increase of stratospheric NO<sub>2</sub> VCDs from GOME-2A to OMI. In this study, we use the GMI  
221 model simulated stratospheric NO<sub>2</sub> VCDs in Figure S3 to calculate the Pandora NO<sub>2</sub> TVCDs. The small

discrepancies between the GMI stratospheric NO<sub>2</sub> VCDs and satellite products do not change the pattern of Pandora NO<sub>2</sub> TVCD diurnal variations or affect the conclusions in this study.

## 2.4 ACAM NO<sub>2</sub> VCD measurements

The ACAM instrument onboard the UC-12 aircraft consists of two thermally spectrometers in the ultraviolet/visible/near-infrared range. The spectrometer in the ultraviolet/visible band (304 nm – 520 nm) with a resolution of 0.8 nm and a sampling of 0.105 nm can be used to detect NO<sub>2</sub> in the atmosphere. The native ground resolution of UC-12 ACAM NO<sub>2</sub> measurements is 0.5 km × 0.75 km at a flight altitude of about 8 km ASL and a nominal ground speed of 100 m s<sup>-1</sup> during the DISCOVER-AQ 2011 campaign (Lamsal et al., 2017), thus providing high-resolution NO<sub>2</sub> VCDs below the aircraft.

In this study, we mainly use the ACAM NO<sub>2</sub> VCD product described by Lamsal et al. (2017), which applied a pair-average co-adding scheme to produce NO<sub>2</sub> VCDs at a ground resolution of about 1.5 km (cross-track) × 1.1 km (along-track) to reduce noise impacts. In their retrieval of ACAM NO<sub>2</sub> VCDs, they first used the DOAS fitting method to generate differential NO<sub>2</sub> SCDs relative to the SCDs at an unpolluted reference location. Then they computed above/below-aircraft AMFs at both sampling and reference locations based on the vector linearized discrete ordinate radiative transfer code (VLIDORT) (Spurr, 2008). In the computation of AMFs, the a priori NO<sub>2</sub> vertical profiles were from a combination of a high-resolution (4-km) CMAQ (the Community Multiscale Air Quality Modeling System) model outputs in the boundary layer and a GMI simulation (2° × 2.5°) results elsewhere in the atmosphere. Finally, the below-aircraft NO<sub>2</sub> VCDs at the sampling locations were generated by dividing below-aircraft NO<sub>2</sub> SCDs at the sampling locations by the corresponding below-aircraft AMFs. The below-aircraft NO<sub>2</sub> SCDs were the differences between the total and above-aircraft NO<sub>2</sub> SCDs. The total NO<sub>2</sub> SCDs were the sum of DOAS fitting generated differential NO<sub>2</sub> SCDs and NO<sub>2</sub> SCDs at the reference location, and the above-aircraft NO<sub>2</sub> SCDs were derived based on above-aircraft AMFs, GMI NO<sub>2</sub> profiles, and

OMNO<sub>2</sub> stratospheric NO<sub>2</sub> VCDs (Lamsal et al., 2017). The ACAM NO<sub>2</sub> VCD product had been evaluated via comparisons with other independent observations during the DISCOVER-AQ 2011 campaign, such as P-3B aircraft, Pandora, and OMNO<sub>2</sub>, and the uncertainty of individual below-aircraft NO<sub>2</sub> VCD is about 30% (Lamsal et al., 2017). To keep the consistency of ACAM NO<sub>2</sub> VCDs, we exclude NO<sub>2</sub> VCDs measured at altitudes < 8 km ASL, which accounts for about 6.8% of the total available ACAM NO<sub>2</sub> VCD data. We regrid the 1.5 km × 1.1 km ACAM NO<sub>2</sub> VCDs to the 4-km REAM grid cells (Figure 1), which are then used to evaluate the distribution of NO<sub>2</sub> VCDs in the 4-km REAM simulation. As a supplement in section 3.7, we also assess the 4-km REAM simulation by using the UC-12 ACAM NO<sub>2</sub> VCDs produced by the Smithsonian Astrophysical Observatory (SAO) algorithms, archived on <https://www-air.larc.nasa.gov/cgi-bin/ArcView/discover-aq.dc-2011?UC12=1#LIU.XIONG/> (last access: December 31, 2019) (Liu et al., 2015a; Liu et al., 2015b). This product is an early version of the SAO algorithm used to produce the Geostationary Trace gas and Aerosol Sensor Optimization (GeoTASO) and the GEOstationary Coastal and Air Pollution Events (GEO-CAPE) Airborne Simulator (GCAS) airborne observations in later airborne campaigns (Nowlan et al., 2016; Nowlan et al., 2018).

## 2.5 Surface NO<sub>2</sub> and O<sub>3</sub> measurements

The measurement of NO<sub>x</sub> is based on the chemiluminescence of electronically excited NO<sub>2</sub><sup>\*</sup>, produced from the reaction of NO with O<sub>3</sub>, and the strength of the chemiluminescence from the decay of NO<sub>2</sub><sup>\*</sup> to NO<sub>2</sub> is proportional to the number of NO molecules present (Reed et al., 2016). NO<sub>2</sub> concentrations can be measured with this method by converting NO<sub>2</sub> to NO first through catalytic reactions (typically on the surface of heated molybdenum oxide (MoO<sub>x</sub>) substrate) or photolytic processes (Lamsal et al., 2015; Reed et al., 2016). However, for the catalytic method, reactive nitrogen compounds other than NO<sub>x</sub> (NO<sub>z</sub>), such as HNO<sub>3</sub>, peroxyacetyl nitrate (PAN), and other organic nitrates, can also be reduced to NO on the heated surface, thus causing an overestimation of NO<sub>2</sub>. The magnitude of the overestimation depends on the concentrations and the reduction

266 efficiencies of interference species, both of which are uncertain. The photolytic approach, which employs  
267 broadband photolysis of ambient NO<sub>2</sub>, offers more accurate NO<sub>2</sub> measurements (Lamsal et al., 2015).

268 There were 11 NO<sub>x</sub> monitoring sites operating in the DISCOVER-AQ region during the campaign (Figure  
269 1), including those from the EPA Air Quality System (AQS) monitoring network and those deployed for the  
270 DISCOVER-AQ campaign. Nine of them measured NO<sub>2</sub> concentrations by a catalytic converter. The other two  
271 sites (Edgewood and Padonia) had NO<sub>2</sub> measurements from both catalytic and photolytic methods. Different  
272 stationary catalytic instruments were used during the campaign: Thermo Electron 42C-Y NO<sub>y</sub> analyzer, Thermo  
273 Model 42C NO<sub>x</sub> analyzer, Thermo Model 42I-Y NO<sub>y</sub> analyzer, and Ecotech Model 9843/9841 T-NO<sub>y</sub> analyzers.  
274 In addition, a mobile platform — NATIVE (Nittany Atmospheric Trailer and Integrated Validation Experiment)  
275 with a Thermo Electron 42C-Y NO<sub>y</sub> analyzer installed, was also deployed in the Edgewood site. The photolytic  
276 measurements of NO<sub>2</sub> in Edgewood and Padonia were from Teledyne API model 200eup photolytic NO<sub>x</sub>  
277 analyzers. We scale catalytic NO<sub>2</sub> measurements using the diurnal ratios of NO<sub>2</sub> photolytic measurements to NO<sub>2</sub>  
278 from the corresponding catalytic analyzers (Figure 4). Figure 4 shows the lowest photolytic/catalytic ratios in the  
279 afternoon, which reflects the production of nitrates and other reactive nitrogen compounds from NO<sub>x</sub> in the  
280 daytime. When photolytic measurements are available, we only use the photolytic observations in this study;  
281 otherwise, we use the scaled catalytic measurements.

282 Nineteen surface O<sub>3</sub> monitoring sites were operating in the DISCOVER-AQ region during the campaign  
283 (Figure 1). They measured O<sub>3</sub> concentrations by using a Federal Equivalent Method (FEM) based on the UV  
284 absorption of O<sub>3</sub> (<https://www.arb.ca.gov/aaqm/qa/qa-manual/vol4/chapter603.pdf>, last access: April 6, 2019)  
285 with an uncertainty of 5 ppb.

## 286 2.6 Aircraft measurements of NO<sub>2</sub> vertical profiles

287 In this study, we mainly use the NO<sub>2</sub> concentrations measured by the National Center for Atmospheric  
288 Research (NCAR) 4-channel chemiluminescence instrument (P-CL) onboard the P-3B aircraft for the evaluation  
289 of REAM simulated NO<sub>2</sub> vertical profiles. The instrument has a NO<sub>2</sub> measurement uncertainty of 10% – 15% and  
290 a 1-second, 1-sigma detection limit of 30 pptv.

291 NO<sub>2</sub> measurements from aircraft spirals provide us with NO<sub>2</sub> vertical profiles. Figure 1 shows the locations  
292 of the aircraft spirals during the DISCOVER-AQ campaign, except for the Chesapeake Bay spirals over the  
293 ocean. There were only six spirals available over the Chesapeake Bay, which have ignorable impacts on the  
294 following analyses. Therefore, we do not use them in this study. The rest 239 spirals in the daytime for July 2011  
295 are used to compute the average profiles of NO<sub>2</sub> for the six inland sites (Figure 1).

296 The aircraft measurements were generally sampled from about a height of 300 m AGL in the boundary layer  
297 to 3.63 km AGL in the free troposphere. We bin these measurements to REAM vertical levels. In order to make  
298 up the missing observations between the surface and 300 m, we apply quadratic polynomial regressions by using  
299 aircraft data below 1 km and coincident NO<sub>2</sub> surface measurements.

300 In addition to using NO<sub>2</sub> concentrations from the NCAR 4-channel instrument to evaluate REAM simulated  
301 NO<sub>2</sub> vertical profiles, we also use P-3B NO, NO<sub>2</sub>, and NO<sub>y</sub> concentrations measured by the NCAR 4-channel  
302 instrument and NO<sub>2</sub>, total peroxyacyl nitrates ( $\Sigma$ PNs), total alkyl nitrates ( $\Sigma$ ANs) (include alkyl nitrates and  
303 hydroxyalkyl nitrates), and HNO<sub>3</sub> concentrations measured by the thermal dissociation-laser induced  
304 fluorescence (TD-LIF) technique (Day et al., 2002; Thornton et al., 2000; Wooldridge et al., 2010) to evaluate the  
305 concentrations of NO<sub>y</sub> from REAM (Table 1). All these P-3B measurements are vertically binned to REAM grid  
306 cells for comparisons with REAM results. In addition, below the P-3B spirals, four NO<sub>y</sub> observation sites at

307 Padonia, Edgewood, Beltsville, and Aldino were operating to provide continuous hourly  $\text{NO}_y$  surface  
308 concentrations during the campaign, which we also use to evaluate REAM simulated  $\text{NO}_y$  surface concentrations  
309 in this study. We summarize the information of available observations at the 11 inland Pandora sites in Table S1.

## 310 **3 Results and discussion**

### 311 3.1 Evaluation of WRF simulated meteorological fields

312 We evaluate the performances of the 36-km and nested 4-km WRF simulations using temperature, potential  
313 temperature, relative humidity (RH), and wind measurements from the P-3B spirals (Figure 1) and precipitation  
314 data from the NCEP (National Centers for Environmental Prediction) Stage IV precipitation dataset. Generally,  
315 P-3B spirals range from ~300 m to ~3.63 km in height above the ground level (AGL). As shown in Figure S4,  
316 both the 36-km and nested 4-km WRF simulations simulate temperature well with  $R^2 = 0.98$ . Both WRF  
317 simulations show good agreement with P-3B measurements in U-wind (36-km:  $R^2 = 0.77$ ; 4-km:  $R^2 = 0.76$ ), V-  
318 wind (36-km:  $R^2 = 0.79$ ; 4-km:  $R^2 = 0.78$ ), wind speed (36-km:  $R^2 = 0.67$ ; 4-km:  $R^2 = 0.67$ ), and wind direction  
319 (36-km:  $R^2 = 0.46$ ; 4-km:  $R^2 = 0.52$ ) (Figures S4 and S5). We further compare the temporal evolutions of vertical  
320 profiles for temperature, potential temperature, RH, U-wind, and V-wind below 3 km from the P-3B observations  
321 with those from the 36-km and nested 4-km WRF simulations in Figure S6. Both WRF simulations well capture  
322 the temporospatial variations of P-3B observed vertical profiles except that RH below 1.5 km is significantly  
323 underestimated during 9:00 – 17:00 LT in both WRF simulations. The evaluations above suggest that WRF  
324 simulated wind fields are good and comparable at 4-km and 36-km resolutions, but potential dry biases exist in  
325 both WRF simulations.

326 The NCEP Stage IV precipitation dataset provides hourly precipitation across the contiguous United States  
327 (CONUS) with a resolution of ~4 km based on the merging of rain gauge data and radar observations (Lin and

328 Mitchell, 2005; Nelson et al., 2016). The Stage IV dataset is useful for evaluating model simulations, satellite  
329 precipitation estimates, and radar precipitation estimates (Davis et al., 2006; Gourley et al., 2011; Kalinga and  
330 Gan, 2010; Lopez, 2011; Yuan et al., 2008). We obtain the Stage IV precipitation data for July 2011 from the  
331 NCAR/UCAR Research Data Archive (<https://rda.ucar.edu/datasets/ds507.5/>, last access: December 28, 2019).  
332 As shown in Figures S7 and S8, generally, both the 36-km and nested 4-km WRF simulations generally predict  
333 much less precipitation (in precipitation amount and duration) compared to the Stage-IV data in July 2011 around  
334 the DISCOVER-AQ campaign region, especially for the nested 4-km WRF simulation, consistent with the  
335 aforementioned underestimated RH and dry bias in WRF simulations. The precipitation biases in the WRF model  
336 will affect REAM simulations of trace gases, leading to high biases of soluble species due to underestimated wet  
337 scavenging. Clouds interfere with satellite observations. Therefore, the precipitation bias does not affect model  
338 evaluations with satellite measurements of NO<sub>2</sub>. Aircraft measurements were also taken in non-precipitating days.

### 339 3.2 Effect of boundary layer vertical mixing on the diurnal variations of surface NO<sub>2</sub> concentrations

#### 340 3.2.1 36-km model simulation in comparison to the surface observations

341 Figures 5a and 5b show the observed and 36-km REAM simulated diurnal cycles of surface NO<sub>2</sub> and O<sub>3</sub>  
342 concentrations on weekdays in July 2011 in the DISCOVER-AQ region. REAM with WRF-YSU simulated  
343 vertical diffusion coefficient ( $k_{zz}$ ) values significantly overestimates NO<sub>2</sub> concentrations and underestimates O<sub>3</sub>  
344 concentrations at night, although it captures the patterns of the diurnal cycles of surface NO<sub>2</sub> and O<sub>3</sub>: an O<sub>3</sub> peak  
345 and a NO<sub>2</sub> minimum around noontime. Here, YSU denotes the Yonsei University planetary boundary layer (PBL)  
346 scheme (Shin and Hong, 2011) used by our WRF simulations (Table S2). At night, the reaction of O<sub>3</sub> + NO → O<sub>2</sub>  
347 + NO<sub>2</sub> produces NO<sub>2</sub> but removes O<sub>3</sub>. Since most NO<sub>x</sub> emissions are in the form of NO, the model biases of low  
348 O<sub>3</sub> and high NO<sub>2</sub> occur at the same time. Since there are no significant chemical sources of O<sub>3</sub> at night, mixing of  
349 O<sub>3</sub> rich air above the surface is the main source of O<sub>3</sub> supply near the surface. Therefore, the nighttime model



biases with WRF-YSU simulated  $k_{zz}$  data in Figure 5 indicate that vertical mixing may be underestimated at night.

During the DISCOVER-AQ campaign, WRF simulated vertical wind velocities are very low at night and have little impact on vertical mixing (Figure S9a). The nighttime vertical mixing is mainly attributed to turbulent mixing. In the YSU scheme, boundary layer  $k_{zz}$  is correlated to PBLH. However, Breuer et al. (2014) and Hu et al. (2012) found that the YSU scheme underestimated nighttime PBLHs in WRF, which is consistent with Figure 6 showing that WRF-YSU  $k_{zz}$ -determined PBLHs are significantly lower than lidar observations in the late afternoon and at night at the UMBC site during the DISCOVER-AQ campaign. Here, the  $k_{zz}$ -determined PBLH refers to the mixing height derived by comparing  $k_{zz}$  to its background values (Hong et al., 2006) but not the PBLH outputs from WRF. The lidar mixing depth data were derived from the Elastic Lidar Facility (ELF) attenuated backscatter signals by using the covariance wavelet transform method and had been validated against radiosonde measurements, Radar wind profiler observations, and Sigma Space mini-micropulse lidar data (Compton et al., 2013). To improve nighttime PBLHs and vertical mixing in REAM, we increase  $k_{zz}$  below 500 m during 18:00 – 5:00 LT to  $5 \text{ m s}^{-2}$  if the WRF-YSU computed  $k_{zz} < 5 \text{ m s}^{-2}$ , which significantly increases the  $k_{zz}$ -determined PBLHs at night (Figure 6), leading to the decreases of simulated surface  $\text{NO}_2$  and the increases of surface  $\text{O}_3$  concentrations at night (Figure 5). The assigned value of  $5 \text{ m s}^{-2}$  is arbitrary. Changing this value to 2 or  $10 \text{ m s}^{-2}$  can also alleviate the biases of model simulated nighttime surface  $\text{NO}_2$  and  $\text{O}_3$  concentrations (Figure S10). An alternative solution to correct the model nighttime simulation biases is to reduce  $\text{NO}_x$  emissions by 50-67%, but we cannot find good reasons to justify this level of  $\text{NO}_x$  emission reduction only at night.

The updated REAM simulation of surface  $\text{NO}_2$  diurnal pattern in Figure 5a is in good agreement with previous studies (Anderson et al., 2014; David and Nair, 2011; Gaur et al., 2014; Reddy et al., 2012; Zhao et al., 2019). Daytime surface  $\text{NO}_2$  concentrations are much lower compared to nighttime, and  $\text{NO}_2$  concentrations

reach a minimum around noontime. As shown in Figure S11, under the influence of vertical turbulent mixing, the surface-layer  $\text{NO}_x$  emission diurnal pattern is similar to the surface  $\text{NO}_2$  diurnal cycle in Figure 5a, emphasizing the importance of turbulent mixing on modulating surface  $\text{NO}_2$  diurnal variations. The highest boundary layer (Figure 6) due to solar radiation leads to the lowest surface-layer  $\text{NO}_x$  emissions (Figure S11) and, therefore, the smallest surface  $\text{NO}_2$  concentrations occur around noontime (Figure 5a). Transport, which is mainly attributed to advection and turbulent mixing, is another critical factor affecting surface  $\text{NO}_2$  diurnal variations (Figure S11). The magnitudes of transport fluxes (Figure S11) are proportional to horizontal and vertical gradients of  $\text{NO}_x$  concentrations and are therefore generally positively correlated to surface  $\text{NO}_2$  concentrations. However, some exceptions exist, reflecting different strengths of advection (U, V, and W) and turbulent mixing ( $k_{zz}$ ) at different times. For example, in the early morning,  $\text{NO}_2$  surface concentrations peak at 5:00 – 6:00 LT (Figure 5a), while transport fluxes peak at 7:00 – 8:00 LT (Figure S11). The delay of the peak is mainly due to lower turbulent mixing at 5:00 – 6:00 LT than other daytime hours in the model (Figure 6). Chemistry also contributes to surface  $\text{NO}_2$  diurnal variations mainly through photochemical sinks in the daytime and  $\text{N}_2\text{O}_5$  hydrolysis at nighttime. Chemistry fluxes in Figure S11 are not only correlated to the strength of photochemical reactions and  $\text{N}_2\text{O}_5$  hydrolysis (chemistry fluxes per unit  $\text{NO}_x$ ) but are also proportional to  $\text{NO}_x$  surface concentrations. Therefore, chemistry fluxes in Figure S11 cannot directly reflect the impact of solar radiation on photochemical reactions. It can, however, still be identified by comparing afternoon chemistry contributions: from 13:00 to 15:00 LT, surface-layer  $\text{NO}_x$  emissions and  $\text{NO}_2$  concentrations are increasing (Figures S11 and 5a); however, chemistry losses are decreasing as a result of the reduction of photochemical sinks with weakening solar radiation. The contributions of vertical mixing and photochemical sinks to  $\text{NO}_2$  concentrations can be further corroborated by daytime variations of  $\text{NO}_2$  vertical profiles and TVCDs discussed in sections 3.3 and 3.4.

Figure 5c shows the diurnal variation on weekends is also simulated well in the improved 36-km model. The diurnal variation of surface  $\text{NO}_2$  concentrations (REAM: 1.5 – 10.2 ppb; observations: 2.1 – 9.8 ppb) is lower

395 than on weekdays (REAM: 2.4 – 12.2 ppb; observations: 3.3 – 14.5 ppb), reflecting lower magnitude and  
396 variation of NO<sub>x</sub> emissions on weekends (Figure 3). Figure 5d also shows an improved simulation of surface O<sub>3</sub>  
397 concentrations at nighttime due to the improved PBLH simulation (Figure 6).

### 398 3.2.2 4-km model simulation in comparison to the surface observations

399 The results of 4-km REAM simulations with original WRF-YSU  $k_{zz}$  (not shown) are very similar to Figure 5  
400 since WRF simulated nocturnal vertical mixing is insensitive to the model horizontal resolution. Applying the  
401 modified nocturnal mixing in the previous section also greatly reduced the nighttime NO<sub>2</sub> overestimate and O<sub>3</sub>  
402 underestimate in the 4-km REAM simulations. All the following analyses are based on REAM simulations with  
403 improved nocturnal mixing. Figure 7 shows that mean surface NO<sub>2</sub> concentrations simulated in the 4-km model  
404 are higher than the 36-km results over Padonia, Oldtown, Essex, Edgewood, Beltsville, and Aldino (Table S1),  
405 leading to generally higher biases compared to the observations in the daytime. A major cause is that the  
406 observation sites are located in regions of high NO<sub>x</sub> emissions (Figure 2). At a higher resolution of 4 km, the high  
407 emissions around the surface sites are apparent compared to rural regions. At the coarser 36-km resolution,  
408 spatial averaging greatly reduces the emissions around the surface sites. On average, NO<sub>x</sub> emissions (molecules  
409 km<sup>-2</sup> s<sup>-1</sup>) around the six surface NO<sub>2</sub> observations sites are 67% higher in the 4-km than the 36-km REAM  
410 simulations (Table S1). The resolution dependence of model results will be further discussed in the model  
411 evaluations using the other in situ and remote sensing measurements.

### 412 3.3 Diurnal variations of NO<sub>2</sub> vertical profiles

413 Figures 8a and 8c show the temporal variations of P-3B observed and 36-km REAM simulated NO<sub>2</sub> vertical  
414 profiles in the daytime on weekdays during the DISCOVER-AQ campaign. 36-km REAM reproduces well the  
415 observed characteristics of NO<sub>2</sub> vertical profiles in the daytime ( $R^2 = 0.89$ ), which are strongly affected by

vertical mixing and photochemistry (Zhang et al., 2016). When vertical mixing is weak in the early morning (6:00 – 8:00 LT), NO<sub>2</sub>, released mainly from surface NO<sub>x</sub> sources, is concentrated in the surface layer, and the vertical gradient is large. As vertical mixing becomes stronger after 8:00 LT, NO<sub>2</sub> concentrations below 500 m decrease significantly, while those over 500 m increase from 6:00 – 8:00 LT to 12:00 – 14:00 LT. It is noteworthy that PBLHs and NO<sub>x</sub> emissions are comparable between 12:00 – 14:00 LT and 15:00 – 17:00 LT (Figures 3 and 6); however, NO<sub>2</sub> concentrations at 15:00 – 17:00 LT are significantly higher than at 12:00 – 14:00 LT in the whole boundary layer, reflecting the impact of the decreased photochemical loss of NO<sub>x</sub> in the late afternoon. In fact, photochemical losses affect all the daytime NO<sub>2</sub> vertical profiles, which can be easily identified by NO<sub>2</sub> TVCD process diagnostics discussed in section 3.4 (Figure 9).

Figures 8b and 8d also show the observed and 36-km REAM simulated vertical profiles on weekends. Similar to Figures 5 and 7, observed and simulated concentrations of NO<sub>2</sub> are lower on weekends than on weekdays. Some of the variations from weekend profiles are due to a lower number of observations (47 spirals) on weekends. The overall agreement between the observed vertical profiles and 36-km model results is good on weekends ( $R^2 = 0.87$ ). At 15:00 – 17:00 LT, the model simulates a larger gradient than what the combination of aircraft and surface measurements indicates. It may be related to the somewhat underestimated PBLHs in the late afternoon in the model (Figure 6).

On weekdays, most simulated vertical profiles at the 4-km resolution (Figure 8e) are similar to 36-km results in part because the average NO<sub>x</sub> emissions over the six P-3B spiral sites are about the same, 4% lower in the 4-km than the 36-km REAM simulations (Table S1). A clear exception is the 4-km REAM simulated vertical profile at 15:00 – 17:00 LT when the model greatly overestimates boundary layer NO<sub>x</sub> mixing and concentrations. The main reason is that WRF simulated vertical velocities ( $w$ ) in the late afternoon are much larger in the 4-km simulation than the 36-km simulation (Figure S9), which can explain the simulated fully mixed

boundary layer at 15:00 – 17:00 LT. Since it is not designed to run at the 4-km resolution and it is commonly assumed that convection can be resolved explicitly at high resolutions, the Kain-Fritsch (new Eta) convection scheme is not used in the nested 4-km WRF simulation (Table S2); it may be related to the large vertical velocities in the late afternoon when thermal instability is the strongest. Appropriate convection parameterization is likely still necessary for 4-km simulations (Zheng et al., 2016), which may also help alleviate the underestimation of precipitation in the nested 4-km WRF simulation as discussed in section 3.1.

The same rapid boundary-layer mixing due to vertical transport is present in the 4-km REAM simulated weekend vertical profile (Figure 8f), although the mixing height is lower. Fewer spirals (47) and distinct transport effect due to different NO<sub>2</sub> horizontal gradients between the 4-km and 36-km REAM simulations (discussed in detail in Section 3.6) may cause the overestimation of weekend profiles in the 4-km REAM simulation.

### 3.4 Daytime variation of NO<sub>2</sub> TVCDs

We compare satellite, P-3B aircraft, and model-simulated TVCDs with Pandora measurements, which provide continuous daytime observations. The locations of Pandora sites are shown in Table S1 and Figure 1. Among the Pandora sites, four sites are located significantly above the ground level: UMCP (~20 m), UMBC (~30 m), SERC (~40 m), and GSFC (~30 m). The other sites are 1.5 m AGL. To properly compare Pandora to other measurements and model simulations, we calculate the missing TVCDs between the Pandora site heights and ground surface by multiplying the Pandora TVCDs with model-simulated TVCD fractions of the corresponding columns. The resulting correction is 2-21% ( $\frac{1}{1 - \text{missing TVCD percentage}}$ ) for the four sites significantly above the ground surface, but the effect on the averaged daytime TVCD variation of all Pandora sites is small (Figure S12). In the following analysis, we use the updated Pandora TVCD data.

The weekday diurnal variations of NO<sub>2</sub> TVCDs from satellites, Pandora, 4- and 36-km REAM, and the P-3B aircraft are shown in Figure 10a. We calculate aircraft derived TVCDs by using equation (1):

$$TVCD_{aircraft}(t) = \frac{\sum c_{aircraft}(t) \times \rho_{REAM}(t) \times V_{REAM}(t)}{A_{REAM}} \quad (1),$$

where  $t$  is time;  $c_{aircraft}$  (v/v) denotes aircraft NO<sub>2</sub> concentrations (mixing ratios) at each level at time  $t$ ;  $\rho_{REAM}$  (molecules / cm<sup>3</sup>) is the density of air from 36-km REAM at the corresponding level;  $V_{REAM}$  (cm<sup>3</sup>) is the volume of the corresponding 36-km REAM grid cell;  $A_{REAM}$  (cm<sup>2</sup>) is the surface area (36 × 36 km<sup>2</sup>). In the calculation, we only use NO<sub>2</sub> concentrations below 3.63 km AGL because few aircraft measurements were available above this height in the campaign. Missing tropospheric NO<sub>2</sub> above 3.63 km AGL in the aircraft TVCD calculation has little impact on our analyses, as 36-km REAM model simulation shows that 85% ± 7% of tropospheric NO<sub>2</sub> are located below 3.63 km AGL during 6:00 – 17:00 LT in the DISCOVER-AQ region, which is roughly consistent with the GMI model results with 85% - 90% tropospheric NO<sub>2</sub> concentrated below 5 km (Lamsal et al., 2014). It should be noted that only six P-3B spirals are available during the campaign, less than the samplings of 11 inland Pandora sites.

The 4-km REAM simulated NO<sub>2</sub> TVCDs are mostly higher than the 36-km results and the observations in daytime on weekdays (Figure 10a). However, since the standard deviations of the data are much larger than the model difference, the 4- and 36-km model results generally show similar characteristics relative to the observations. REAM simulation results are in reasonable agreement with Pandora, P-3B aircraft, and satellite daytime NO<sub>2</sub> TVCDs, except that NASA-derived OMI (OMNO2) TVCDs are somewhat lower than other datasets, which may be partly due to biased a priori vertical profiles from the GMI model in the NASA retrieval in the campaign (Lamsal et al., 2014; Lamsal et al., 2020). TVCDs derived by using the DOMINO algorithm and 36-km REAM NO<sub>2</sub> vertical profiles are in agreement with those from KNMI, which indicates that the TM4

479 model from KNMI provides reasonable estimates of a priori NO<sub>2</sub> vertical profiles on weekdays in the  
480 DISCOVER-AQ region in summer.

481 We find evident decreases of NO<sub>2</sub> TVCDs from GOME-2A to OMI in Figure 10a, which is consistent with  
482 Pandora, REAM results, and previous studies that showed decreasing NO<sub>2</sub> TVCDs from SCIAMACHY to OMI  
483 due to photochemical losses in summer (Boersma et al., 2008; Boersma et al., 2009). P-3B aircraft TVCDs also  
484 show this decrease feature but have large variations due in part to the limited aircraft sampling data.

485 Pandora NO<sub>2</sub> TVCD data have different characteristics from REAM simulated and P-3B aircraft measured  
486 TVCDs at 5:00 – 7:00 LT and 14:00 – 18:00 LT (Figure 10a). At 5:00 – 7:00 LT, Pandora data show a significant  
487 increase of NO<sub>2</sub> TVCDs, but REAM and aircraft TVCDs generally decrease except for 4-km REAM TVCDs  
488 with a slight increase from 6:00 – 7:00 LT on weekdays. At 14:00 LT – 18:00 LT, Pandora TVCDs have little  
489 variations, but REAM and aircraft TVCDs increase significantly. The relatively flat Pandora TVCDs in the late  
490 afternoon compared to REAM and P-3B aircraft measurements are consistent with Lamsal et al. (2017), which  
491 found the significant underestimation (26% – 30%) of Pandora VCDs compared to UC-12 ACAM measurements  
492 from 16:00 LT to 18:00 LT during the DISCOVER-AQ campaign. We show the simulated effects of emission,  
493 chemistry, transport, and dry deposition on NO<sub>x</sub> TVCDs in Figure 9. The simulated early morning slight decrease  
494 of NO<sub>2</sub> TVCDs is mainly due to the chemical transformation between NO<sub>2</sub> and NO favoring the accumulation of  
495 NO under low-O<sub>3</sub> and low-HO<sub>2</sub>/RO<sub>2</sub> conditions, thus NO TVCDs increase significantly but NO<sub>2</sub> TVCDs  
496 continue decreasing slowly during the period. The increase in the late afternoon is primarily due to the decrease  
497 of photochemistry-related sinks. The reasons for the discrepancies of NO<sub>2</sub> TVCDs between Pandora and REAM  
498 results during the above two periods are unclear. Large SZAs in the early morning and the late afternoon (Figure  
499 S1) lead to the higher uncertainties of Pandora measurements (Herman et al., 2009), although we have excluded  
500 Pandora measurements with SZA > 80°. In addition, Pandora is a sun-tracking instrument with a small effective

501 FOV and is sensitive to local conditions within a narrow spatial range which may differ significantly from the  
502 average properties of 36- and 4-km grid cells depending upon the time of the day (Figure S13) (Herman et al.,  
503 2009; Herman et al., 2018; Herman et al., 2019; Judd et al., 2018; Judd et al., 2019; Judd et al., 2020; Lamsal et  
504 al., 2017; Reed et al., 2015). As we mentioned above, ~85% tropospheric NO<sub>2</sub> are located below 3.63 km in the  
505 DISCOVER-AQ 2011 region based on the 36-km REAM simulation results. The Pandora FOV of 1.6° is  
506 approximately equivalent to a nadir horizontal extension of only 0.1 km ( $2 \times 3.63 \text{ km} \times \tan \frac{1.6}{2} = 0.1 \text{ km}$ ) at  
507 3.63 km AGL and 30 m at 1.0 km AGL. Therefore, Pandora measures different air columns of NO<sub>2</sub> at different  
508 times of the day, especially in the morning and afternoon when SZA is large, as shown in Figure S13.  
509 Considering the potential spatial heterogeneity of boundary-layer NO<sub>2</sub>, it is possible that the morning (east),  
510 noontime (nadir), afternoon (west) NO<sub>2</sub> VCDs are significantly different from each other. Unlike Pandora,  
511 satellites and aircraft are far from the ground surface and cover large areas; therefore, the impact of SZA on their  
512 NO<sub>2</sub> VCD measurements is insignificant compared to Pandora measurements. Another possible reason is that  
513 Pandora instruments had few observations in the early morning, and the resulting average may not be  
514 representative (Figure S2).

515 To further understand the daytime variation of NO<sub>2</sub> TVCDs, we examine P-3B aircraft data derived and  
516 REAM simulated NO<sub>2</sub> VCD variations for different height bins (Figure 11). NO<sub>2</sub> VCDs below 3.63 km AGL  
517 display a “U”-shaped pattern from 5:00 LT to 17:00 LT. In the morning, as vertical mixing becomes stronger  
518 after sunrise, high-NO<sub>x</sub> air in the lower layer is mixed with low-NO<sub>x</sub> air in the upper layer. The increase of NO<sub>x</sub>  
519 vertical mixing above 300 m is sufficient to counter the increase of photochemical loss in the morning.  
520 Conversely, the NO<sub>2</sub> VCDs below 300 m decrease remarkably from sunrise (about 6:00 LT) to around noontime  
521 due to both vertical mixing and the increase of photochemical strength. From 13:00 LT to 16:00 LT, NO<sub>2</sub> VCDs  
522 increase slowly, reflecting a relative balance among emissions, transport, chemistry, and dry depositions. The



sharp jump of the VCDs from 16:00 LT to 17:00 LT is mainly due to dramatically reduced chemical loss. And 4-km REAM simulated NO<sub>2</sub> VCDs at 0.30-3.63 km at 16:00-17:00 LT are much higher than 36-km results partly because of the rapid vertical mixing in the 4-km REAM simulation (Figures 8 and S9).

Similar to NO<sub>2</sub> surface concentrations and vertical profiles in Figures 7 and 8, the NO<sub>2</sub> TVCD variation is also smaller on weekends than on weekdays, but the day-night pattern is similar (Figure 10). Although the 4-km REAM NO<sub>2</sub> TVCDs are generally higher than the 36-km results and observations in the daytime, considering their large standard deviations, NO<sub>2</sub> TVCDs from both simulations are comparable to satellite products, Pandora, and P-3B aircraft observations most of the time on weekends. The exception is that Pandora TVCDs have different variation patterns in the early morning and late afternoon from REAM simulations, similar to those found on weekdays.

### 3.5 Model comparisons with NO<sub>y</sub> measurements

NO<sub>y</sub> is longer-lived than NO<sub>x</sub>, and NO<sub>y</sub> concentrations are not affected by chemistry as much as NO<sub>x</sub>. We obtain two types of NO<sub>y</sub> concentrations from the P-3B aircraft in the DISCOVER-AQ campaign: one is NO<sub>y</sub> concentrations directly measured by the NCAR 4-channel instrument, corresponding to the sum of NO, NO<sub>2</sub>, ΣPNs, ΣANs, HNO<sub>3</sub>, N<sub>2</sub>O<sub>5</sub>, HNO<sub>4</sub>, HONO, and the other reactive nitrogenic species in REAM (all the other species are described in Table 1); the other one, which we name as “derived-NO<sub>y</sub>”, is the sum of NO from the NCAR 4-channel instrument and NO<sub>2</sub> (NO<sub>2</sub>\_LIF), ΣPNs, ΣANs, and HNO<sub>3</sub> measured by the TD-LIF technique, corresponding to NO, NO<sub>2</sub>, ΣPNs, ΣANs, and HNO<sub>3</sub> in REAM (Table 1). On average, P-3B derived-NO<sub>y</sub> concentrations ( $2.88 \pm 2.24$  ppb) are 17% higher than coincident P-3B NO<sub>y</sub> concentrations ( $2.46 \pm 2.06$  ppb) with  $R^2 = 0.75$ , generally reflecting consistency between these two types of measurements. As shown in Table 1, on weekdays, the 36-km REAM NO<sub>y</sub> concentrations are 45% larger than P-3B with  $R^2 = 0.33$ , and the 36-km REAM derived-NO<sub>y</sub> concentrations are 8% larger than P-3B with  $R^2 = 0.41$ . 4-km REAM show similar results,

545 suggesting that REAM simulations generally reproduce the observed  $\text{NO}_y$  and derived- $\text{NO}_y$  concentrations within  
546 the uncertainties, although the average values from REAM are somewhat larger than the observations due in part  
547 to the underestimate of precipitation in the WRF model simulations resulting in underestimated wet scavenging  
548 of  $\text{HNO}_3$  in REAM. The concentrations of weekday  $\text{NO}$ ,  $\text{NO}_2$ , and  $\Sigma\text{PNs}$  from REAM simulations are also  
549 comparable to the observations. However, weekday  $\Sigma\text{ANs}$  concentrations are 68% lower in the 36-km REAM  
550 than observations, suggesting that the chemistry mechanism in REAM may need further improvement to better  
551 represent isoprene nitrates. It is noteworthy that, since  $\Sigma\text{ANs}$  only account for a small fraction ( $\sim 11\%$ ) in  
552 observed derived- $\text{NO}_y$ , the absolute difference between REAM simulated and P-3B observed  $\Sigma\text{ANs}$   
553 concentrations is still small compared to  $\text{HNO}_3$ . Weekday  $\text{HNO}_3$  concentrations are significantly higher in  
554 REAM simulations (36-km: 57%, 0.65 ppb; 4-km: 74%, 0.86 ppb) than P-3B observations, which is the main  
555 reason for the somewhat larger  $\text{NO}_y$  and derived- $\text{NO}_y$  concentrations in REAM compared to P-3B observations.  
556 The higher  $\text{HNO}_3$  concentrations in REAM may be related to the underestimation of precipitation in the  
557 corresponding WRF simulations, as discussed in section 3.1 (Figures S7 and S8), leading to the underestimated  
558 wet scavenging of  $\text{HNO}_3$ , especially for the 4-km REAM simulation.

559 We also examine the weekday diurnal variations of derived- $\text{NO}_y$  vertical profiles from P-3B and REAM  
560 simulations in Figure S14. Generally, both 36- and 4-km REAM simulations capture the variation characteristics  
561 of observed vertical profiles, which are similar to those for  $\text{NO}_2$  in Figure 8. REAM derived- $\text{NO}_y$  concentrations  
562 are comparable to P-3B observations at most vertical levels on weekdays. Some larger derived- $\text{NO}_y$   
563 concentrations in the model results can be partially explained by larger  $\text{HNO}_3$  concentrations in REAM, such as  
564 those below 1 km at 9:00 – 11:00 LT for the 36-km REAM and those below 2.0 km at 12:00 – 17:00 LT for the  
565 4-km REAM (Figure S15).

Figure 12 shows the comparison of the diurnal cycles of surface  $\text{NO}_y$  concentrations observed at Padonia, Edgewood, Beltsville, and Aldino during the DISCOVER-AQ campaign with those from the REAM simulations. Generally, the REAM simulations reproduce the observed surface  $\text{NO}_y$  diurnal cycles except for the spikes around 17:00 – 20:00 LT due to still underestimated PBLHs (Figure 6). 4-km simulation results have a higher bias than 36-km results relative to the observations in the daytime, similar to the comparisons of  $\text{NO}_2$  surface concentrations and TVCDs in Figures 7 and 10 due to higher emissions around the observation sites in 4- than 36-km simulations (Table S1 and Figure 2).

### 3.6 Resolution dependence of $\text{NO}_x$ emission distribution

We show previously that the 4-km REAM simulated  $\text{NO}_2$  and  $\text{NO}_y$  surface concentrations and  $\text{NO}_2$  TVCDs are higher than observations in the daytime in comparison to the corresponding 36-km REAM results (Figures 7, 10, and 12). An examination of monthly mean  $\text{NO}_2$  surface concentrations and TVCDs for July 2011 also shows that 4-km simulation results are significantly higher than the 36-km results over the 11 inland Pandora sites in the daytime (Figure 13). The process-level diagnostics in Figure 9 indicate that the mean contribution of  $\text{NO}_x$  emissions to  $\text{NO}_x \Delta\text{TVCDs}$  in the 4-km simulation is  $1.32 \times 10^{15} \text{ molecules cm}^{-2} \text{ h}^{-1}$  larger than that in the 36-km simulation between 9:00 LT and 16:00 LT, while the absolute mean contributions of chemistry and transport (they are negative in Figure 9, so we use absolute values here) in the 4-km simulation are  $0.26 \times 10^{15}$  and  $0.87 \times 10^{15} \text{ molecules cm}^{-2} \text{ h}^{-1}$  larger than the 36-km simulation, respectively. The contributions of dry deposition to  $\text{NO}_x \Delta\text{TVCDs}$  are negligible compared to other factors in both simulations (Figure 9). Therefore, the 34% higher  $\text{NO}_x$  emissions over the 11 inland Pandora sites (Table S1 and Figure 3) is the main reason for the larger daytime  $\text{NO}_2$  surface concentrations and TVCDs in the 4-km than the 36-km REAM simulations (Figure 13). The significantly different contribution changes between  $\text{NO}_x$  emissions ( $1.32 \times 10^{15} \text{ molecules cm}^{-2} \text{ h}^{-1}$  or about one third) and chemistry ( $0.26 \times 10^{15} \text{ molecules cm}^{-2} \text{ h}^{-1}$  or about 8%) reflect potential chemical nonlinearity (Li et al., 2019; Silvern et al., 2019; Valin et al., 2011) and transport effect. Different transport contributions between the 4-

589 km and the 36-km REAM are mainly caused by their different NO<sub>x</sub> horizontal gradients (Figures 2, 14, and 15),  
590 while the impact of wind fields is small since we do not find significant differences in horizontal wind  
591 components between the two simulations except for some lower wind speeds below 1000 m for the 36-km WRF  
592 simulation compared to the nested 4-km WRF simulation (Figure S16). Our sensitivity tests with the WRF  
593 Single-Moment 3-class (WSM3) simple ice scheme (not shown) can improve the wind speed comparison below  
594 1000 m between the 36-km and nested 4-km WRF simulations but still produce similar NO<sub>x</sub> simulation results as  
595 WSM6 shown here. Therefore, the somewhat lower wind speeds below 1000 m in the 36-km WRF simulation are  
596 not the reason for the difference between the 4-km and 36-km REAM simulations. The impact of transport on the  
597 two REAM simulations can be further verified by the comparison of NO<sub>2</sub> TVCDs over the six P-3B spiral sites  
598 between the two simulations (Figure S17). Mean NO<sub>x</sub> emissions over the six P-3B spiral sites are close (relative  
599 difference < 4%) between the two simulations (Table S1 and Figure S17). From 9:00 to 12:00 LT, the  
600 contributions of NO<sub>x</sub> emissions to NO<sub>x</sub> ΔTVCDs are  $2.50 \times 10^{15}$  and  $2.49 \times 10^{15}$  molecules cm<sup>-2</sup> h<sup>-1</sup> for the 36-km  
601 and 4-km REAM simulations, respectively, and the contributions of chemistry are also close between the two  
602 simulations (36-km:  $-2.62 \times 10^{15}$  molecules cm<sup>-2</sup> h<sup>-1</sup>; 4-km:  $-2.69 \times 10^{15}$  molecules cm<sup>-2</sup> h<sup>-1</sup>). However, the  
603 contributions of transport are  $-0.39 \times 10^{15}$  and  $0.03 \times 10^{15}$  molecules cm<sup>-2</sup> h<sup>-1</sup> for the 36-km and 4-km REAM  
604 simulations, respectively, leading to larger NO<sub>2</sub> TVCDs in the 4-km REAM simulation than the 36-km REAM  
605 from 9:00 – 12:00 LT (Figure S17c). Since horizontal wind fields over the six P-3B spiral sites are comparable  
606 between two simulations (Figures S4, S5, S6, and S16) and larger NO<sub>x</sub> horizontal gradients are found near the P-  
607 3B spiral sites for the 4-km REAM (Figure 2), we attribute the different transport contributions between the two  
608 simulations to a much larger NO<sub>x</sub> emission gradient around the measurement locations in 4-km than 36-km  
609 emission distributions.

610 We re-grid the 4-km REAM results into the grid cells of the 36-km REAM, which can significantly reduce  
611 the impact of different NO<sub>x</sub> emission distributions and associated transport on the two simulations. Compared to

the original 4-km REAM results, the re-gridded surface NO<sub>2</sub> concentrations and TVCDs over the 11 inland Pandora sites are much closer to the 36-km REAM results (Figure 13). After re-gridding the 4-km REAM results into 36-km REAM grid cells, we also find more comparable NO<sub>y</sub> surface concentrations between the re-gridded 4-km results and the 36-km REAM results (Figure S18). The remaining discrepancies between the re-gridded results and the 36-km REAM results may be due to chemical nonlinearity and other meteorological effects, such as larger vertical wind in the 4-km REAM (Figure S9) and their different  $k_{zz}$  values in the PBL. Although other factors, such as chemical nonlinearity and vertical diffusion, may affect the 36-km and 4-km REAM simulations differently, the difference between 4- and 36-km simulations of reactive nitrogen is largely due to that of NO<sub>x</sub> emissions.

The 4- and 36-km simulation difference depends on the location of the observations. In some regions, the NO<sub>x</sub> emission difference between 4- and 36-km simulations is small. The comparison of NO<sub>y</sub> measurements from P-3B spirals with coincident REAM results in Table 1 suggests that the 4-km and 36-km REAM simulations produce similar NO<sub>y</sub> (relative difference ~4%) and derived-NO<sub>y</sub> (relative difference ~6%) concentrations on weekdays, and both simulation results are comparable to the observations. The NO<sub>y</sub> similarity over the P-3B spiral sites between the 36-km and 4-km REAM simulations is consistent with the comparable NO<sub>x</sub> emissions over (relative difference < 4%) the six P-3B spiral sites between the two simulations (Table S1). The differences between the 4-km model simulation results and P3-B observations are larger on weekends than on weekdays (Table 1) due to the limited weekend sampling since model simulated monthly mean values show similar differences between the 4-km and 36-km REAM simulations on weekends as on weekdays (not shown).

### 3.7 Evaluation of 36- and 4-km NO<sub>x</sub> distribution with OMI, GOME-2A, and ACAM measurements

The evaluation of model simulations of surface, aircraft, and satellite observations tends to point out a high bias in 4- than 36-km model simulations. We note that this comparison is based on the averages of multiple sites.

634 NO<sub>x</sub> emissions at individual sites are not always higher in the 4-km than 36-km REAM, such as SERC, Fairhill,  
635 and Essex, with much higher 36-km NO<sub>x</sub> emissions than 4-km NO<sub>x</sub> emissions (Table S1). We conduct  
636 individual-site comparisons of surface NO<sub>2</sub> concentrations, surface NO<sub>y</sub> concentrations, NO<sub>2</sub> vertical profiles,  
637 derived-NO<sub>y</sub> vertical profiles, and NO<sub>2</sub> TVCDs of the 36-km REAM and the 4-km REAM results relative to the  
638 corresponding observations in Figures S19 – S23. The 36-km simulation results can be larger, smaller, or  
639 comparable to the 4-km simulation results, and both simulations can produce higher, lower, or similar results as  
640 the observations for different variables at different sites. The varying model biases depending on the observation  
641 site reflect the different spatial distributions of NO<sub>x</sub> emissions between the 36- and 4-km REAM simulations  
642 (Figure 2) and suggest potential distribution biases of NO<sub>x</sub> emissions in both simulations.

643 Here we examine the 4-km model simulated NO<sub>2</sub> VCDs with high-resolution ACAM measurements onboard  
644 the UC-12 aircraft in Figures 14 and S24, respectively. The spatial distributions of ACAM and 4-km REAM NO<sub>2</sub>  
645 VCDs are generally consistent with  $R^2 = 0.35$  on weekdays and  $R^2 = 0.50$  on weekends. The domain averages of  
646 ACAM and 4-km REAM NO<sub>2</sub> VCDs are  $4.7 \pm 2.0$  and  $4.6 \pm 3.2 \times 10^{15}$  molecules cm<sup>-2</sup> on weekdays and  $3.0 \pm$   
647  $1.7$  and  $3.3 \pm 2.7 \times 10^{15}$  molecules cm<sup>-2</sup> on weekends, respectively. The spatial distributions of ACAM and 4-km  
648 REAM NO<sub>2</sub> VCDs are highly correlated with the spatial distribution of 4-km NEI2011 NO<sub>x</sub> emissions. All three  
649 distributions capture two strong peaks around Baltimore and Washington, D.C. urban regions and another weak  
650 peak in the northeast corner of the domain (Wilmington city in Delaware) (Figures 14 and S24). However,  
651 Figures 14 and S24 clearly show that NO<sub>2</sub> VCDs from the 4-km REAM simulation are more concentrated in  
652 Baltimore and Washington, D.C. urban regions than ACAM, which are also reflected by the higher NO<sub>2</sub> VCD  
653 standard deviations of the 4-km REAM results than ACAM. Several Pandora sites are in the highest NO<sub>2</sub> VCD  
654 regions where the 4-km REAM generally produces larger NO<sub>2</sub> VCDs than ACAM, which explains why the NO<sub>2</sub>  
655 TVCDs over the 11 Pandora sites from the 4-km REAM simulation are higher than the observations (Figure 10)  
656 and the 36-km REAM results (Figure 13) around noontime. Horizontal transport cannot explain the NO<sub>2</sub> VCD

distribution biases in the 4-km REAM simulation due to the following reasons. Firstly, horizontal wind fields are simulated as well by the nested 4-km WRF simulation as the 36-km WRF compared to P-3B measurements, as discussed in section 3.1. Secondly, the prevailing northwest wind in the daytime (Figure S5) should move  $\text{NO}_x$  eastward, but we find no significant eastward shift of  $\text{NO}_2$  VCDs compared to  $\text{NO}_x$  emissions in both ACAM and 4-km REAM distributions (Figure 14). Lastly, we find a local minimum of  $\text{NO}_2$  VCDs in the middle of the Baltimore urban region (the purple circle in Figure 14b) in the ACAM distribution, which cannot be explained by horizontal transport or chemical nonlinearity due to the surrounding high  $\text{NO}_x$  emissions in the 4-km REAM simulation. Therefore, we attribute the distribution inconsistency between ACAM and the 4-km REAM to the distribution biases of NEI2011  $\text{NO}_x$  emissions at the 4-km resolution since the average below-aircraft  $\text{NO}_2$  VCDs between ACAM and the 4-km REAM are about the same.

It is noteworthy that about 91% ACAM  $\text{NO}_2$  VCD data are measured from 8:00 – 16:00 LT, and only using ACAM  $\text{NO}_2$  VCDs between 8:00 and 16:00 LT for the above comparison does not affect our results shown here. Moreover, to minimize the effect of overestimated afternoon vertical mixing (Figure 8) on the 4-km REAM simulation results, we also examine the comparison between ACAM  $\text{NO}_2$  VCDs from 9:00 – 14:00 LT with coincident 4-km REAM results, which produces similar results as shown here.

We also evaluate the  $\text{NO}_2$  VCD distributions from the 4-km REAM simulation on weekdays and weekends with ACAM  $\text{NO}_2$  VCDs below the U-12 aircraft obtained from <https://www-air.larc.nasa.gov/cgi-bin/ArcView/discover-aq.dc-2011?UC12=1#LIU.XIONG/> in Figures S25 and S26. Although the domain mean ACAM  $\text{NO}_2$  VCDs in Figures S25 and S26 are higher than coincident 4-km REAM results due to the different retrieval method from Lamsal et al. (2017), such as different above-aircraft  $\text{NO}_2$  VCDs and different a priori  $\text{NO}_2$  vertical profiles, we can still find clear distribution inconsistencies between the 4-km REAM and ACAM  $\text{NO}_2$  VCDs. The 4-km REAM  $\text{NO}_2$  VCDs are more concentrated in the Baltimore and Washington, D.C. urban regions

679 than this set of ACAM data, which is consistent with the conclusions derived from the ACAM dataset retrieved  
680 by Lamsal et al. (2017).

681 The potential distribution bias of the NEI2011 NO<sub>x</sub> emissions at 36-km resolution is analyzed by comparing  
682 the 36-km REAM simulated NO<sub>2</sub> TVCDs with those retrieved by OMI and GOME-2A, as shown in Figures 15  
683 (OMI, 13:00 LT) and S27 (GOME-2A, 9:30 LT). Both KNMI and our retrievals based on the 36-km REAM NO<sub>2</sub>  
684 vertical profiles show that OMI and GOME-2A NO<sub>2</sub> TVCDs have lower spatial variations than the corresponding  
685 36-km REAM simulation results. OMI and GOME-2A retrievals have lower NO<sub>2</sub> TVCDs around the Baltimore  
686 and Washington, D.C. urban regions and higher values in relatively rural regions than the 36-km REAM. The  
687 distribution bias of the 36-km REAM NO<sub>2</sub> TVCDs is also identified on weekends through their comparison with  
688 OMI and GOME-2A retrievals (not shown). The good agreement between simulated and observed wind suggests  
689 that the model horizontal transport error cannot explain such an urban-rural contrast between satellite  
690 observations and 36-km REAM simulation results. However, two caveats deserve attention. Firstly, the 36-km  
691 REAM cannot resolve urban areas as detailed as the 4-km REAM (Figure 14), and urban and rural regions may  
692 coexist in one 36-km grid cell. Secondly, the OMI and GOME-2A pixels can be much larger than 36-km REAM  
693 grid cells, possibly leading to more spatially homogenous distributions of satellite NO<sub>2</sub> TVCD data.

### 694 3.8 Implications for NO<sub>x</sub> emissions

695 The analysis of section 3.7 indicates that the NEI2011 NO<sub>x</sub> emission distributions at 36- and 4-km  
696 resolutions are likely biased for the Baltimore-Washington region. The distribution bias of NO<sub>x</sub> emission  
697 inventories is corroborated by the comparison of the NO<sub>x</sub> emission inventory derived from the CONSolidated  
698 Community Emissions Processor Tool, Motor Vehicle (CONCEPT MV) v2.1 with that estimated by the Sparse  
699 Matrix Operator Kernel Emissions (SMOKE) v3.0 model with the Motor Vehicle Emissions Simulator (MOVES)  
700 v2010a (DenBleyker et al., 2012). CONCEPT with finer vehicle activity information as input produced a wider-



701 spread but less-concentrated running exhaust NO<sub>x</sub> emissions compared to MOVES in the Denver urban area for  
702 July 2008 (DenBleyker et al., 2012). In addition, Canty et al. (2015) found that CMAQ 4.7.1, with on-road  
703 emissions from MOVES and off-road emissions from the National Mobile Inventory Model (NMIM),  
704 overestimated NO<sub>2</sub> TVCD over urban regions and underestimated NO<sub>2</sub> TVCDs over rural areas in the  
705 northeastern U.S. for July and August 2011 compared to the OMNO2 product. The urban-rural contrast was also  
706 found in Texas during the 2013 DISCOVER-AQ campaign in the studies of Souri et al. (2016) and Souri et al.  
707 (2018), implying distribution uncertainties in NO<sub>x</sub> emissions, although these studies and Canty et al. (2015)  
708 focused more on polluted regions with overestimated NO<sub>x</sub> emissions in their conclusions. The emission  
709 distribution bias may also explain why Anderson et al. (2014) have different results from our simulated  
710 concentrations in Table 1. In their study, they compared in-situ observations with a nested CMAQ simulation  
711 with a resolution of 1.33 km. It is difficult to build up a reliable emission inventory for the whole U.S. at very  
712 high resolutions with currently available datasets due to the significant inhomogeneity of NO<sub>x</sub> emissions (Marr et  
713 al., 2013), but we can still expect significant improvements of the temporal-spatial distributions of NO<sub>x</sub> emissions  
714 in the near future as GPS-based information start to be used in the NEI estimates (DenBleyker et al., 2017).

715 Here, we emphasize that our study is not necessarily contradictory to recent studies concerning the  
716 overestimation of NEI NO<sub>x</sub> emissions (Anderson et al., 2014; Canty et al., 2015; McDonald et al., 2018; Souri et  
717 al., 2016; Souri et al., 2018; Travis et al., 2016). Different types of observations in different periods and locations  
718 are analyzed for various purposes. This study focuses more on the spatial distribution of NO<sub>x</sub> emissions in  
719 NEI2011, while previous studies are concerned more about the NO<sub>x</sub> emission magnitudes in highly polluted sites,  
720 although the spatial distribution issue was also mentioned in some of the studies. If we limit our analyses to those  
721 observations in Figures 7, 10, and 12 and the 4-km REAM, we would also conclude an overestimation of NEI  
722 NO<sub>x</sub> emissions. Considering the significant heterogeneity of NO<sub>x</sub> emissions, the spatial distribution of NO<sub>x</sub>  
723 emissions is a critical factor in evaluating NO<sub>x</sub> emissions and improving emission estimation and air quality

724 models, which deserves more attention in future studies, especially when chemical and transport models are  
725 moving to higher and higher resolutions.

## 726 **4 Conclusions**

727 We investigate the diurnal cycles of surface NO<sub>2</sub> concentrations, NO<sub>2</sub> vertical profiles, and NO<sub>2</sub> TVCDs  
728 using REAM model simulations on the basis of the observations from air quality monitoring sites, aircraft,  
729 Pandora, OMI, and GOME-2A during the DISCOVER-AQ 2011 campaign. We find that WRF simulated  
730 nighttime  $k_{zz}$ -determined PBLHs are significantly lower than ELF lidar measurements. Increasing nighttime  
731 mixing from 18:00 – 5:00 LT in the REAM simulations, we significantly improve REAM simulations of  
732 nighttime surface NO<sub>2</sub> and O<sub>3</sub> concentrations.

733 The REAM simulation reproduces well the observed regional mean diurnal cycles of surface NO<sub>2</sub> and NO<sub>y</sub>  
734 concentrations, NO<sub>2</sub> vertical profiles, and NO<sub>2</sub> TVCDs on weekdays. Observed NO<sub>2</sub> concentrations in the  
735 boundary layer and TVCDs on weekends are significantly lower than on weekdays. By specifying a weekend to  
736 weekday NO<sub>x</sub> emission ratio of 2:3 and applying a less variable NO<sub>x</sub> emission diurnal profile on weekends than  
737 weekdays, REAM can simulate well the weekend observations. Two issues are also noted. First, Pandora TVCDs  
738 show different variations from aircraft-derived and REAM-simulated TVCDs in the early morning and late  
739 afternoon, which may be due to the uncertainties of Pandora measurements at large SZAs and the small effective  
740 FOV of Pandora. Second, the weekday OMI NO<sub>2</sub> TVCDs derived by NASA are somewhat lower than the KNMI  
741 OMI product, P-3B aircraft-derived TVCDs, Pandora, and REAM results; the difference may be caused by the a  
742 priori vertical profiles used in the NASA retrieval.

743 While a higher-resolution simulation is assumed to be superior at a priori, the large observation dataset  
744 during DISCOVER-AQ 2011 offers the opportunity of a detailed comparison of 4-km and 36-km model

745 simulations. Through the comparison, we find two areas that have not been widely recognized. The first is not  
746 using convection parameterization in high-resolution WRF simulations since convection can be resolved  
747 explicitly and most convection parameterizations are not designed for high-resolution simulations. We find that  
748 4-km WRF tends to overestimate boundary-layer mixing and vertical transport in the late afternoon, leading to a  
749 high model bias in simulated NO<sub>2</sub> vertical profiles compared to P-3B aircraft observations. The reasons for this  
750 late-afternoon bias in 4-km WRF simulations and model modifications to mitigate this bias need further studies.

751 A second issue is related to the spatial distribution of NO<sub>x</sub> emissions in NEI2011. In general, the 4-km  
752 simulation results tend to have a high bias relative to the 36-km results on the regional mean observations.  
753 However, for individual sites, relative to the 36-km model simulations, the 4-km model results can show larger,  
754 smaller, or similar biases compared to the observations depending upon observation location. Based on process  
755 diagnostics and analyses, we find that the bias discrepancies between the 36-km and 4-km REAM simulations are  
756 mainly attributed to their different NO<sub>x</sub> emissions and their spatial gradients at different sites. The comparison of  
757 4-km ACAM NO<sub>2</sub> VCD measurements from the UC-12 aircraft with coincident 4-km REAM results shows that  
758 4-km REAM NO<sub>2</sub> VCDs are more concentrated in urban regions than the ACAM observations. OMI and GOME-  
759 2A data also show less spatially varying NO<sub>2</sub> TVCD distributions with lower NO<sub>2</sub> TVCDs around the Baltimore-  
760 Washington urban regions and higher TVCDs in surrounding rural areas than corresponding 36-km REAM  
761 simulation results. Further model analysis indicates that the 36- and 4-km VCD discrepancies are due primarily to  
762 the distribution bias of NEI2011 NO<sub>x</sub> emissions at 36- and 4-km resolutions. Our results highlight the research  
763 need to improve the methodologies and datasets to improve the spatial distributions in emission estimates.

#### 764 **Data availability**

765 The DISCOVER-AQ 2011 campaign datasets are archived on [https://www-air.larc.nasa.gov/cgi-](https://www-air.larc.nasa.gov/cgi-bin/ArcView/discover-aq.dc-2011)  
766 [bin/ArcView/discover-aq.dc-2011](https://www-air.larc.nasa.gov/cgi-bin/ArcView/discover-aq.dc-2011) (last access: March 14, 2021). EPA air quality monitoring datasets are from

767 <https://www3.epa.gov/airdata/> (last access: June 23, 2015). The NASA OMI NO<sub>2</sub> product is from  
768 [https://disc.gsfc.nasa.gov/datasets/OMNO2\\_003/summary](https://disc.gsfc.nasa.gov/datasets/OMNO2_003/summary) (last access: September 26, 2020). The KNMI OMI  
769 NO<sub>2</sub> product is from <http://www.temis.nl/airpollution/no2.html> (last access: January 14, 2015). We obtain the  
770 KNMI GOME-2A NO<sub>2</sub> VCD archives from [http://www.temis.nl/airpollution/no2col/no2colgome2\\_v2.php](http://www.temis.nl/airpollution/no2col/no2colgome2_v2.php) (last  
771 access: January 22, 2015). The GMI MERRA-2 simulation results are from  
772 [https://portal.nccs.nasa.gov/datashare/dirac/gmidata2/users/mrdamon/Hindcast-](https://portal.nccs.nasa.gov/datashare/dirac/gmidata2/users/mrdamon/Hindcast-Family/HindcastMR2/2011/stations/)  
773 [Family/HindcastMR2/2011/stations/](https://portal.nccs.nasa.gov/datashare/dirac/gmidata2/users/mrdamon/Hindcast-Family/HindcastMR2/2011/stations/) (last access: May 14, 2019). We obtain the UC-12 ACAM NO<sub>2</sub> VCD  
774 product by X. Liu from [https://www-air.larc.nasa.gov/cgi-bin/ArcView/discover-aq.dc-](https://www-air.larc.nasa.gov/cgi-bin/ArcView/discover-aq.dc-2011?UC12=1#LIU.XIONG/)  
775 [2011?UC12=1#LIU.XIONG/](https://www-air.larc.nasa.gov/cgi-bin/ArcView/discover-aq.dc-2011?UC12=1#LIU.XIONG/) (last access: December 31, 2019). The Stage IV precipitation data is downloaded  
776 from <https://rda.ucar.edu/datasets/ds507.5/> (last access: December 28, 2019). The NCEP CFSv2 6-hourly product  
777 is available at <http://rda.ucar.edu/datasets/ds094.0/> (last access: March 10, 2015). REAM simulation results for  
778 this study and the UC-12 ACAM NO<sub>2</sub> VCD product by Lamsal et al. (2017) are available upon request.

## 779 **Author contribution**

780 JL and YW designed the study. JL, RZ, and CS updated the REAM model. JL conducted model simulations.  
781 KFB developed the DOMINO algorithm, CS applied the algorithm to REAM vertical profiles, and JL updated the  
782 retrieval algorithm and did the retrieval by using REAM NO<sub>2</sub> vertical profiles. AW, JH, EAC, RWL, JJS, RD,  
783 AMT, TNK, LNL, SJJ, MGK, XL, CRN made various measurements in the DISCOVER-AQ 2011 campaign. JL  
784 conducted the analyses with discussions with YW, RZ, CS, AW, JH, KFB, EAC, RWL, JJS, RD, AMT, TNK,  
785 LNL, SJJ, MGK, XL, and CRN. JL and YW led the writing of the manuscript with inputs from all other  
786 coauthors. All coauthors reviewed the manuscript.

## 787 **Competing interests**

788 The authors declare that they have no conflict of interest.

789    **Acknowledgments**

790    This work was supported by the NASA ACMAP Program. We thank Chun Zhao for providing us the PNNL  
791    NEI2011 emission inventory. We thank Yuzhong Zhang and Jenny Fisher for providing the updated GEOS-  
792    Chem chemistry mechanism files and thank Yuzhong Zhang, Yongjia Song, Hang Qu, Ye Cheng, Aoxing Zhang,  
793    Yufei Zou and Ziming Ke for discussion with J. Li. We thank Susan Strahan for providing the GMI outputs  
794    download link.

## 795    **References**

- 796    Anderson, D. C., Loughner, C. P., Diskin, G., Weinheimer, A., Canty, T. P., Salawitch, R. J., Worden, H. M.,  
797    Fried, A., Mikoviny, T., and Wisthaler, A.: Measured and modeled CO and NO<sub>y</sub> in DISCOVER-AQ: An  
798    evaluation of emissions and chemistry over the eastern US, *Atmos. Environ.*, 96, 78-87,  
799    <https://doi.org/10.1016/j.atmosenv.2014.07.004>, 2014.
- 800    Beirle, S., Platt, U., Wenig, M., and Wagner, T.: Weekly cycle of NO<sub>2</sub> by GOME measurements: A signature of  
801    anthropogenic sources, *Atmos. Chem. Phys.*, 3, 2225-2232, <https://doi.org/10.5194/acp-3-2225-2003>, 2003.
- 802    Boersma, K. F., Eskes, H. J., Veefkind, J. P., Brinksma, E. J., Van Der A, R. J., Sneep, M., Van Den Oord, G. H.  
803    J., Levelt, P. F., Stammes, P., and Gleason, J. F.: Near-real time retrieval of tropospheric NO<sub>2</sub> from OMI, *Atmos.*  
804    *Chem. Phys.*, 7, 2103-2118, <https://doi.org/10.5194/acp-7-2103-2007>, 2007.
- 805    Boersma, K. F., Jacob, D. J., Eskes, H. J., Pinder, R. W., Wang, J., and Van Der A, R. J.: Intercomparison of  
806    SCIAMACHY and OMI tropospheric NO<sub>2</sub> columns: Observing the diurnal evolution of chemistry and emissions  
807    from space, *J. Geophys. Res.-Atmos.*, 113, <https://doi.org/10.1029/2007JD008816>, 2008.
- 808    Boersma, K. F., Jacob, D. J., Trainic, M., Rudich, Y., De Smedt, I., Dirksen, R., and Eskes, H. J.: Validation of  
809    urban NO<sub>2</sub> concentrations and their diurnal and seasonal variations observed from the SCIAMACHY and OMI  
810    sensors using in situ surface measurements in Israeli cities, *Atmos. Chem. Phys.*, 9, 3867-3879,  
811    <https://doi.org/10.5194/acp-9-3867-2009>, 2009.
- 812    Boersma, K. F., Eskes, H. J., Dirksen, R. J., Veefkind, J. P., Stammes, P., Huijnen, V., Kleipool, Q. L., Sneep,  
813    M., Claas, J., and Leitão, J.: An improved tropospheric NO<sub>2</sub> column retrieval algorithm for the Ozone Monitoring  
814    Instrument, *Atmos. Meas. Tech.*, 4, 1905-1928, <https://doi.org/10.5194/amt-4-1905-2011>, 2011.
- 815    Boersma, K. F., Eskes, H. J., Richter, A., De Smedt, I., Lorente, A., Beirle, S., van Geffen, J. H., Zara, M., Peters,  
816    E., and Roozendaal, M. V.: Improving algorithms and uncertainty estimates for satellite NO<sub>2</sub> retrievals: results  
817    from the quality assurance for the essential climate variables (QA4ECV) project, *Atmos. Meas. Tech.*, 11, 6651-  
818    6678, <https://doi.org/10.5194/amt-11-6651-2018>, 2018.
- 819    Breuer, H., Ács, F., Horváth, Á., Németh, P., and Rajkai, K.: Diurnal course analysis of the WRF-simulated and  
820    observation-based planetary boundary layer height, *Advances in Science and Research*, 11, 83-88,  
821    <https://doi.org/10.5194/asr-11-83-2014>, 2014.
- 822    Brohede, S., McLinden, C. A., Berthet, G., Haley, C. S., Murtagh, D., and Sioris, C. E.: A stratospheric NO<sub>2</sub>  
823    climatology from Odin/OSIRIS limb-scatter measurements, *Can. J. Phys.*, 85, 1253-1274,  
824    <https://doi.org/10.1139/p07-141>, 2007.
- 825    Brown, S. S., Dibb, J. E., Stark, H., Aldener, M., Vozella, M., Whitlow, S., Williams, E. J., Lerner, B. M.,  
826    Jakoubek, R., and Middlebrook, A. M.: Nighttime removal of NO<sub>x</sub> in the summer marine boundary layer,  
827    *Geophys. Res. Lett.*, 31, <https://doi.org/10.1029/2004GL019412>, 2004.

828 Bucselá, E. J., Krotkov, N. A., Celarier, E. A., Lamsal, L. N., Swartz, W. H., Bhartia, P. K., Boersma, K. F.,  
829 Veefkind, J. P., Gleason, J. F., and Pickering, K. E.: A new stratospheric and tropospheric NO<sub>2</sub> retrieval  
830 algorithm for nadir-viewing satellite instruments: applications to OMI, *Atmos. Meas. Tech.*, 6, 2607-2626,  
831 <https://doi.org/10.5194/amt-6-2607-2013>, 2013.

832 Canty, T., Hembeck, L., Vinciguerra, T., Goldberg, D., Carpenter, S., Allen, D., Loughner, C., Salawitch, R., and  
833 Dickerson, R.: Ozone and NO<sub>x</sub> chemistry in the eastern US: evaluation of CMAQ/CB05 with satellite (OMI)  
834 data, *Atmos. Chem. Phys.*, 15, 10965, <https://doi.org/10.5194/acp-15-10965-2015>, 2015.

835 Chance, K.: OMI Algorithm Theoretical Basis Document: OMI Trace Gas Algorithms, available at  
836 <https://ozoneaq.gsfc.nasa.gov/media/docs/ATBD-OMI-04.pdf>, Smithsonian Astrophysical Observatory,  
837 Cambridge, MA, USA2.0, 78, 2002.

838 Cheng, Y., Wang, Y., Zhang, Y., Chen, G., Crawford, J. H., Kleb, M. M., Diskin, G. S., and Weinheimer, A. J.:  
839 Large biogenic contribution to boundary layer O<sub>3</sub>-CO regression slope in summer, *Geophys. Res. Lett.*, 44, 7061-  
840 7068, <https://doi.org/10.1002/2017GL074405>, 2017.

841 Cheng, Y., Wang, Y., Zhang, Y., Crawford, J. H., Diskin, G. S., Weinheimer, A. J., and Fried, A.: Estimator of  
842 surface ozone using formaldehyde and carbon monoxide concentrations over the eastern United States in  
843 summer, *J. Geophys. Res.-Atmos.*, 123, 7642-7655, <https://doi.org/10.1029/2018JD028452>, 2018.

844 Choi, S., Lamsal, L. N., Follette-Cook, M., Joiner, J., Krotkov, N. A., Swartz, W. H., Pickering, K. E., Loughner,  
845 C. P., Appel, W., Pfister, G., Saide, P. E., Cohen, R. C., Weinheimer, A. J., and Herman, J. R.: Assessment of  
846 NO<sub>2</sub> observations during DISCOVER-AQ and KORUS-AQ field campaigns, *Atmos. Meas. Tech.*, 13, 2523-  
847 2546, <https://doi.org/10.5194/amt-13-2523-2020>, 2020.

848 Choi, Y., Wang, Y., Zeng, T., Cunnold, D., Yang, E. S., Martin, R., Chance, K., Thouret, V., and Edgerton, E.:  
849 Springtime transitions of NO<sub>2</sub>, CO, and O<sub>3</sub> over North America: Model evaluation and analysis, *J. Geophys.*  
850 *Res.-Atmos.*, 113, <https://doi.org/10.1029/2007JD009632>, 2008.

851 Choi, Y., Kim, H., Tong, D., and Lee, P.: Summertime weekly cycles of observed and modeled NO<sub>x</sub> and O<sub>3</sub>  
852 concentrations as a function of satellite-derived ozone production sensitivity and land use types over the  
853 Continental United States, *Atmos. Chem. Phys.*, 12, 6291-6307, <https://doi.org/10.5194/acp-12-6291-2012>, 2012.

854 Compton, J. C., Delgado, R., Berkoff, T. A., and Hoff, R. M.: Determination of planetary boundary layer height  
855 on short spatial and temporal scales: A demonstration of the covariance wavelet transform in ground-based wind  
856 profiler and lidar measurements, *Journal of Atmospheric and Oceanic Technology*, 30, 1566-1575,  
857 <https://doi.org/10.1175/JTECH-D-12-00116.1>, 2013.

858 David, L. M., and Nair, P. R.: Diurnal and seasonal variability of surface ozone and NO<sub>x</sub> at a tropical coastal site:  
859 Association with mesoscale and synoptic meteorological conditions, *J. Geophys. Res.-Atmos.*, 116,  
860 <https://doi.org/10.1029/2010JD015076>, 2011.

861 Davis, C., Brown, B., and Bullock, R.: Object-based verification of precipitation forecasts. Part I: Methodology  
 862 and application to mesoscale rain areas, *Monthly Weather Review*, 134, 1772-1784,  
 863 <https://doi.org/10.1175/MWR3145.1>, 2006.

864 Day, D. A., Wooldridge, P. J., Dillon, M. B., Thornton, J. A., and Cohen, R. C.: A thermal dissociation laser -  
 865 induced fluorescence instrument for in situ detection of NO<sub>2</sub>, peroxy nitrates, alkyl nitrates, and HNO<sub>3</sub>, *J.*  
 866 *Geophys. Res.-Atmos.*, 107, ACH 4-1-ACH 4-14, <https://doi.org/10.1029/2001JD000779>, 2002.

867 de Foy, B.: City-level variations in NO<sub>x</sub> emissions derived from hourly monitoring data in Chicago, *Atmos.*  
 868 *Environ.*, 176, 128-139, <https://doi.org/10.1016/j.atmosenv.2017.12.028>, 2018.

869 DenBleyker, A., Morris, R. E., Lindhjem, C. E., Parker, L. K., Shah, T., Koo, B., Loomis, C., and Dilly, J.:  
 870 Temporal and Spatial Detail in Mobile Source Emission Inventories for Regional Air Quality Modeling, 2012  
 871 International Emission Inventory Conference, Florida, U.S., August 13 - 16, 2012, 2012.

872 DenBleyker, A., Koupal, J., DeFries, T., and Palacios, C.: Improvement of Default Inputs for MOVES and  
 873 SMOKE-MOVES: CRC Project A-100, available at [https://crcao.org/reports/recentstudies2017/A-](https://crcao.org/reports/recentstudies2017/A-100/ERG_FinalReport_CRCA100_28Feb2017.pdf)  
 874 [100/ERG\\_FinalReport\\_CRCA100\\_28Feb2017.pdf](https://crcao.org/reports/recentstudies2017/A-100/ERG_FinalReport_CRCA100_28Feb2017.pdf), Eastern Research Group, Inc., Austin, TX, 86, 2017.

875 Dirksen, R. J., Boersma, K. F., Eskes, H. J., Ionov, D. V., Bucsela, E. J., Levelt, P. F., and Kelder, H. M.:  
 876 Evaluation of stratospheric NO<sub>2</sub> retrieved from the Ozone Monitoring Instrument: Intercomparison, diurnal cycle,  
 877 and trending, *J. Geophys. Res.-Atmos.*, 116, <https://doi.org/10.1029/2010JD014943>, 2011.

878 EPA: Profile of the 2011 National Air Emissions Inventory, available at  
 879 [https://www.epa.gov/sites/production/files/2015-08/documents/lite\\_finalversion\\_ver10.pdf](https://www.epa.gov/sites/production/files/2015-08/documents/lite_finalversion_ver10.pdf), U.S. Environmental  
 880 Protection Agency, 2014.

881 Fisher, J. A., Jacob, D. J., Travis, K. R., Kim, P. S., Marais, E. A., Chan Miller, C., Yu, K., Zhu, L., Yantosca, R.  
 882 M., and Sulprizio, M. P.: Organic nitrate chemistry and its implications for nitrogen budgets in an isoprene-and  
 883 monoterpene-rich atmosphere: constraints from aircraft (SEAC<sup>4</sup>RS) and ground-based (SOAS) observations in  
 884 the Southeast US, *Atmos. Chem. Phys.*, 16, 5969-5991, <https://doi.org/10.5194/acp-16-5969-2016>, 2016.

885 Flynn, C. M., Pickering, K. E., Crawford, J. H., Lamsal, L., Krotkov, N., Herman, J., Weinheimer, A., Chen, G.,  
 886 Liu, X., and Szykman, J.: Relationship between column-density and surface mixing ratio: Statistical analysis of  
 887 O<sub>3</sub> and NO<sub>2</sub> data from the July 2011 Maryland DISCOVER-AQ mission, *Atmos. Environ.*, 92, 429-441,  
 888 <https://doi.org/10.1016/j.atmosenv.2014.04.041>, 2014.

889 Frey, M. M., Brough, N., France, J. L., Anderson, P. S., Traulle, O., King, M. D., Jones, A. E., Wolff, E. W., and  
 890 Savarino, J.: The diurnal variability of atmospheric nitrogen oxides (NO and NO<sub>2</sub>) above the Antarctic Plateau  
 891 driven by atmospheric stability and snow emissions, *Atmos. Chem. Phys.*, 13, 3045-3062,  
 892 <https://doi.org/10.5194/acp-13-3045-2013>, 2013.

893 Gaur, A., Tripathi, S. N., Kanawade, V. P., Tare, V., and Shukla, S. P.: Four-year measurements of trace gases  
 894 (SO<sub>2</sub>, NO<sub>x</sub>, CO, and O<sub>3</sub>) at an urban location, Kanpur, in Northern India, *Journal of Atmospheric Chemistry*, 71,  
 895 283-301, <https://doi.org/10.1007/s10874-014-9295-8>, 2014.



896 Gourley, J. J., Hong, Y., Flamig, Z. L., Wang, J., Vergara, H., and Anagnostou, E. N.: Hydrologic evaluation of  
897 rainfall estimates from radar, satellite, gauge, and combinations on Ft. Cobb basin, Oklahoma, *Journal of*  
898 *Hydrometeorology*, 12, 973-988, <https://doi.org/10.1175/2011JHM1287.1>, 2011.

899 Guenther, A. B., Jiang, X., Heald, C. L., Sakulyanontvittaya, T., Duhl, T., Emmons, L. K., and Wang, X.: The  
900 Model of Emissions of Gases and Aerosols from Nature version 2.1 (MEGAN2.1): an extended and updated  
901 framework for modeling biogenic emissions, *Geosci. Model Dev.*, 5, 1471-1492, [https://doi.org/10.5194/gmd-5-](https://doi.org/10.5194/gmd-5-1471-2012)  
902 [1471-2012](https://doi.org/10.5194/gmd-5-1471-2012), 2012.

903 Hains, J. C., Boersma, K. F., Kroon, M., Dirksen, R. J., Cohen, R. C., Perring, A. E., Bucsela, E., Volten, H.,  
904 Swart, D. P. J., and Richter, A.: Testing and improving OMI DOMINO tropospheric NO<sub>2</sub> using observations  
905 from the DANDELIONS and INTEx - B validation campaigns, *J. Geophys. Res.-Atmos.*, 115,  
906 <https://doi.org/10.1029/2009JD012399>, 2010.

907 Herman, J., Cede, A., Spinei, E., Mount, G., Tzortziou, M., and Abuhassan, N.: NO<sub>2</sub> column amounts from  
908 ground-based Pandora and MFDOAS spectrometers using the direct-Sun DOAS technique: Intercomparisons and  
909 application to OMI validation, *J. Geophys. Res.-Atmos.*, 114, <https://doi.org/10.1029/2009JD011848>, 2009.

910 Herman, J., Spinei, E., Fried, A., Kim, J., Kim, J., Kim, W., Cede, A., Abuhassan, N., and Segal-Rozenhaimer,  
911 M.: NO<sub>2</sub> and HCHO measurements in Korea from 2012 to 2016 from Pandora spectrometer instruments  
912 compared with OMI retrievals and with aircraft measurements during the KORUS-AQ campaign, *Atmos. Meas.*  
913 *Tech.*, 11, 4583-4603, <https://doi.org/10.5194/amt-11-4583-2018>, 2018.

914 Herman, J., Abuhassan, N., Kim, J., Kim, J., Dubey, M., Raponi, M., and Tzortziou, M.: Underestimation of  
915 column NO<sub>2</sub> amounts from the OMI satellite compared to diurnally varying ground-based retrievals from  
916 multiple PANDORA spectrometer instruments, *Atmos. Meas. Tech.*, 12, 5593-5612, [https://doi.org/10.5194/amt-](https://doi.org/10.5194/amt-12-5593-2019)  
917 [12-5593-2019](https://doi.org/10.5194/amt-12-5593-2019), 2019.

918 Hong, S.-Y., Noh, Y., and Dudhia, J.: A new vertical diffusion package with an explicit treatment of entrainment  
919 processes, *Monthly weather review*, 134, 2318-2341, <https://doi.org/10.1175/MWR3199.1>, 2006.

920 Hu, X., Doughty, D. C., Sanchez, K. J., Joseph, E., and Fuentes, J. D.: Ozone variability in the atmospheric  
921 boundary layer in Maryland and its implications for vertical transport model, *Atmos. Environ.*, 46, 354-364,  
922 <https://doi.org/10.1016/j.atmosenv.2011.09.054>, 2012.

923 Huijnen, V., Eskes, H. J., Poupkou, A., Elbern, H., Boersma, K. F., Foret, G., Sofiev, M., Valdebenito, A.,  
924 Flemming, J., and Stein, O.: Comparison of OMI NO<sub>2</sub> tropospheric columns with an ensemble of global and  
925 European regional air quality models, *Atmos. Chem. Phys.*, 10, 3273-3296, [https://doi.org/10.5194/acp-10-3273-](https://doi.org/10.5194/acp-10-3273-2010)  
926 [2010](https://doi.org/10.5194/acp-10-3273-2010), 2010.

927 Ionov, D. V., Timofeyev, Y. M., Sinyakov, V. P., Semenov, V. K., Goutail, F., Pommereau, J. P., Bucsela, E. J.,  
928 Celarier, E. A., and Kroon, M.: Ground - based validation of EOS - Aura OMI NO<sub>2</sub> vertical column data in the  
929 midlatitude mountain ranges of Tien Shan (Kyrgyzstan) and Alps (France), *J. Geophys. Res.-Atmos.*, 113,  
930 <https://doi.org/10.1029/2007JD008659>, 2008.

931 Irie, H., Kanaya, Y., Akimoto, H., Tanimoto, H., Wang, Z., Gleason, J. F., and Bucsela, E. J.: Validation of OMI  
932 tropospheric NO<sub>2</sub> column data using MAX-DOAS measurements deep inside the North China Plain in June  
933 2006: Mount Tai Experiment 2006, *Atmos. Chem. Phys.*, 8, 6577-6586, <https://doi.org/10.5194/acp-8-6577-2008>,  
934 2008.

935 Irie, H., Boersma, K. F., Kanaya, Y., Takashima, H., Pan, X., and Wang, Z.: Quantitative bias estimates for  
936 tropospheric NO<sub>2</sub> columns retrieved from SCIAMACHY, OMI, and GOME-2 using a common standard for East  
937 Asia, *Atmos. Meas. Tech.*, 5, 2403-2411, <https://doi.org/10.5194/amt-5-2403-2012>, 2012.

938 Jones, A. E., Weller, R., Wolff, E. W., and Jacobi, H. W.: Speciation and rate of photochemical NO and NO<sub>2</sub>  
939 production in Antarctic snow, *Geophys. Res. Lett.*, 27, 345-348, <https://doi.org/10.1029/1999GL010885>, 2000.

940 Judd, L. M., Al-Saadi, J. A., Valin, L. C., Pierce, R. B., Yang, K., Janz, S. J., Kowalewski, M. G., Szykman, J. J.,  
941 Tiefengraber, M., and Mueller, M.: The Dawn of Geostationary Air Quality Monitoring: Case Studies from Seoul  
942 and Los Angeles, *Front. Environ. Sci.*, 6, 85, <https://doi.org/10.3389/fenvs.2018.00085>, 2018.

943 Judd, L. M., Al-Saadi, J. A., Janz, S. J., Kowalewski, M. G., Pierce, R. B., Szykman, J. J., Valin, L. C., Swap, R.,  
944 Cede, A., Mueller, M., Tiefengraber, M., Abuhassan, N., and Williams, D.: Evaluating the impact of spatial  
945 resolution on tropospheric NO<sub>2</sub> column comparisons within urban areas using high-resolution airborne data,  
946 *Atmos. Meas. Tech.*, 12, 6091-6111, <https://doi.org/10.5194/amt-12-6091-2019>, 2019.

947 Judd, L. M., Al-Saadi, J. A., Szykman, J. J., Valin, L. C., Janz, S. J., Kowalewski, M. G., Eskes, H. J., Veeffkind,  
948 J. P., Cede, A., Mueller, M., Gebetsberger, M., Swap, R., Pierce, R. B., Nowlan, C. R., Abad, G. G., Nehrir, A.,  
949 and Williams, D.: Evaluating Sentinel-5P TROPOMI tropospheric NO<sub>2</sub> column densities with airborne and  
950 Pandora spectrometers near New York City and Long Island Sound, *Atmos. Meas. Tech. Discuss.*, 2020, 1-52,  
951 <https://doi.org/10.5194/amt-2020-151>, 2020.

952 Kalinga, O. A., and Gan, T. Y.: Estimation of rainfall from infrared - microwave satellite data for basin - scale  
953 hydrologic modelling, *Hydrological processes*, 24, 2068-2086, <https://doi.org/10.1002/hyp.7626>, 2010.

954 Kaynak, B., Hu, Y., Martin, R. V., Sioris, C. E., and Russell, A. G.: Comparison of weekly cycle of NO<sub>2</sub> satellite  
955 retrievals and NO<sub>x</sub> emission inventories for the continental United States, *J. Geophys. Res.-Atmos.*, 114,  
956 <https://doi.org/10.1029/2008JD010714>, 2009.

957 Kim, S. W., McDonald, B., Baidar, S., Brown, S., Dube, B., Ferrare, R., Frost, G., Harley, R., Holloway, J., and  
958 Lee, H. J.: Modeling the weekly cycle of NO<sub>x</sub> and CO emissions and their impacts on O<sub>3</sub> in the Los Angeles-  
959 South Coast Air Basin during the CalNex 2010 field campaign, *J. Geophys. Res.-Atmos.*, 121, 1340-1360,  
960 <https://doi.org/10.1002/2015JD024292>, 2016.

961 Knepp, T., Pippin, M., Crawford, J., Chen, G., Szykman, J., Long, R., Cowen, L., Cede, A., Abuhassan, N., and  
962 Herman, J.: Estimating surface NO<sub>2</sub> and SO<sub>2</sub> mixing ratios from fast-response total column observations and  
963 potential application to geostationary missions, *Journal of atmospheric chemistry*, 72, 261-286,  
964 <https://doi.org/10.1007/s10874-013-9257-6>, 2015.

965 Kollonige, D. E., Thompson, A. M., Josipovic, M., Tzortziou, M., Beukes, J. P., Burger, R., Martins, D. K., van  
 966 Zyl, P. G., Vakkari, V., and Laakso, L.: OMI Satellite and Ground - Based Pandora Observations and Their  
 967 Application to Surface NO<sub>2</sub> Estimations at Terrestrial and Marine Sites, *J. Geophys. Res.-Atmos.*, 123, 1441-  
 968 1459, <https://doi.org/10.1002/2017JD026518>, 2018.

969 Krotkov, N. A., Lamsal, L. N., Celarier, E. A., Swartz, W. H., Marchenko, S. V., Bucsela, E. J., Chan, K. L.,  
 970 Wenig, M., and Zara, M.: The version 3 OMI NO<sub>2</sub> standard product, *Atmos. Meas. Tech.*, 10, 3133-3149,  
 971 <https://doi.org/10.5194/amt-10-3133-2017>, 2017.

972 Lamsal, L. N., Krotkov, N. A., Celarier, E. A., Swartz, W. H., Pickering, K. E., Bucsela, E. J., Gleason, J. F.,  
 973 Martin, R. V., Philip, S., and Irie, H.: Evaluation of OMI operational standard NO<sub>2</sub> column retrievals using in situ  
 974 and surface-based NO<sub>2</sub> observations, *Atmos. Chem. Phys.*, 14, 11587-11609, [https://doi.org/10.5194/acp-14-](https://doi.org/10.5194/acp-14-11587-2014)  
 975 [11587-2014](https://doi.org/10.5194/acp-14-11587-2014), 2014.

976 Lamsal, L. N., Duncan, B. N., Yoshida, Y., Krotkov, N. A., Pickering, K. E., Streets, D. G., and Lu, Z.: US NO<sub>2</sub>  
 977 trends (2005–2013): EPA Air Quality System (AQS) data versus improved observations from the Ozone  
 978 Monitoring Instrument (OMI), *Atmos. Environ.*, 110, 130-143, <https://doi.org/10.1016/j.atmosenv.2015.03.055>,  
 979 2015.

980 Lamsal, L. N., Janz, S. J., Krotkov, N. A., Pickering, K. E., Spurr, R. J. D., Kowalewski, M. G., Loughner, C. P.,  
 981 Crawford, J. H., Swartz, W. H., and Herman, J.: High - resolution NO<sub>2</sub> observations from the Airborne Compact  
 982 Atmospheric Mapper: Retrieval and validation, *J. Geophys. Res.-Atmos.*, 122, 1953-1970,  
 983 <https://doi.org/10.1002/2016JD025483>, 2017.

984 Lamsal, L. N., Krotkov, N. A., Vasilkov, A., Marchenko, S., Qin, W., Yang, E. S., Fasnacht, Z., Joiner, J., Choi,  
 985 S., Haffner, D., Swartz, W. H., Fisher, B., and Bucsela, E.: OMI/Aura Nitrogen Dioxide Standard Product with  
 986 Improved Surface and Cloud Treatments, *Atmos. Meas. Tech. Discuss.*, 2020, 1-56, [https://doi.org/10.5194/amt-](https://doi.org/10.5194/amt-2020-200)  
 987 [2020-200](https://doi.org/10.5194/amt-2020-200), 2020.

988 Levelt, P. F., Hilsenrath, E., Leppelmeier, G. W., van den Oord, G. H. J., Bhartia, P. K., Tamminen, J., de Haan,  
 989 J. F., and Veeffkind, J. P.: Science objectives of the ozone monitoring instrument, *IEEE Transactions on*  
 990 *Geoscience and Remote Sensing*, 44, 1199-1208, <https://doi.org/10.1109/TGRS.2006.872336>, 2006.

991 Li, J., Wang, Y., and Qu, H.: Dependence of summertime surface ozone on NO<sub>x</sub> and VOC emissions over the  
 992 United States: Peak time and value, *Geophys. Res. Lett.*, 46, 3540-3550, <https://doi.org/10.1029/2018GL081823>,  
 993 2019.

994 Lin, Y., and Mitchell, K. E.: the NCEP stage II/IV hourly precipitation analyses: Development and applications,  
 995 19th Conf. Hydrology, American Meteorological Society, San Diego, CA, USA, 2005,

996 Liu, C., Liu, X., Kowalewski, M., Janz, S., González Abad, G., Pickering, K., Chance, K., and Lamsal, L.:  
 997 Analysis of ACAM data for trace gas retrievals during the 2011 DISCOVER-AQ campaign, *Journal of*  
 998 *Spectroscopy*, 2015, <https://doi.org/10.1155/2015/827160>, 2015a.

999 Liu, C., Liu, X., Kowalewski, M. G., Janz, S. J., González Abad, G., Pickering, K. E., Chance, K., and Lamsal, L.  
1000 N.: Characterization and verification of ACAM slit functions for trace-gas retrievals during the 2011  
1001 DISCOVER-AQ flight campaign, *Atmos. Meas. Tech.*, 8, 751-759, <https://doi.org/10.5194/amt-8-751-2015>,  
1002 2015b.

1003 Liu, Z., Wang, Y., Gu, D., Zhao, C., Huey, L. G., Stickel, R., Liao, J., Shao, M., Zhu, T., and Zeng, L.:  
1004 Summertime photochemistry during CAREBeijing-2007: RO<sub>x</sub> budgets and O<sub>3</sub> formation, *Atmos. Chem. Phys.*,  
1005 12, 7737-7752, <https://doi.org/10.5194/acp-12-7737-2012>, 2012.

1006 Lopez, P.: Direct 4D-Var assimilation of NCEP stage IV radar and gauge precipitation data at ECMWF, *Monthly*  
1007 *Weather Review*, 139, 2098-2116, <https://doi.org/10.1175/2010MWR3565.1>, 2011.

1008 Luo, G., Yu, F., and Schwab, J.: Revised treatment of wet scavenging processes dramatically improves GEOS-  
1009 Chem 12.0.0 simulations of surface nitric acid, nitrate, and ammonium over the United States, *Geosci. Model*  
1010 *Dev.*, 12, 3439-3447, <https://doi.org/10.5194/gmd-12-3439-2019>, 2019.

1011 Marchenko, S., Krotkov, N., Lamsal, L., Celarier, E., Swartz, W., and Bucsela, E.: Revising the slant column  
1012 density retrieval of nitrogen dioxide observed by the Ozone Monitoring Instrument, *J. Geophys. Res.-Atmos.*,  
1013 120, 5670-5692, <https://doi.org/10.1002/2014JD022913>, 2015.

1014 Marr, L. C., Moore, T. O., Klappmeyer, M. E., and Killar, M. B.: Comparison of NO<sub>x</sub> Fluxes Measured by Eddy  
1015 Covariance to Emission Inventories and Land Use, *Environ. Sci. Technol.*, 47, 1800-1808,  
1016 <https://doi.org/10.1021/es303150y>, 2013.

1017 McDonald, B., McKeen, S., Cui, Y. Y., Ahmadov, R., Kim, S.-W., Frost, G. J., Pollack, I., Peischl, J., Ryerson,  
1018 T. B., and Holloway, J.: Modeling Ozone in the Eastern US using a Fuel-Based Mobile Source Emissions  
1019 Inventory, *Environ. Sci. Technol.*, <https://doi.org/10.1021/acs.est.8b00778>, 2018.

1020 Munro, R., Eisinger, M., Anderson, C., Callies, J., Corpaccioli, E., Lang, R., Lefebvre, A., Livschitz, Y., and  
1021 Albinana, A. P.: GOME-2 on MetOp, *Proc. of The 2006 EUMETSAT Meteorological Satellite Conference*,  
1022 Helsinki, Finland, 2006, 48,

1023 Nelson, B. R., Prat, O. P., Seo, D.-J., and Habib, E.: Assessment and implications of NCEP Stage IV quantitative  
1024 precipitation estimates for product intercomparisons, *Weather and Forecasting*, 31, 371-394,  
1025 <https://doi.org/10.1175/WAF-D-14-00112.1>, 2016.

1026 Ng, N. L., Brown, S. S., Archibald, A. T., Atlas, E., Cohen, R. C., Crowley, J. N., Day, D. A., Donahue, N. M.,  
1027 Fry, J. L., and Fuchs, H.: Nitrate radicals and biogenic volatile organic compounds: oxidation, mechanisms, and  
1028 organic aerosol, *Atmos. Chem. Phys.*, 17, 2103-2162, <https://doi.org/10.5194/acp-17-2103-2017>, 2017.

1029 Nowlan, C. R., Liu, X., Leitch, J. W., Chance, K., González Abad, G., Liu, C., Zoogman, P., Cole, J., Delker, T.,  
1030 Good, W., Murcray, F., Ruppert, L., Soo, D., Follette-Cook, M. B., Janz, S. J., Kowalewski, M. G., Loughner, C.  
1031 P., Pickering, K. E., Herman, J. R., Beaver, M. R., Long, R. W., Szykman, J. J., Judd, L. M., Kelley, P., Luke, W.  
1032 T., Ren, X., and Al-Saadi, J. A.: Nitrogen dioxide observations from the Geostationary Trace gas and Aerosol  
1033 Sensor Optimization (GeoTASO) airborne instrument: Retrieval algorithm and measurements during

1034 DISCOVER-AQ Texas 2013, Atmos. Meas. Tech., 9, 2647-2668, <https://doi.org/10.5194/amt-9-2647-2016>,  
1035 2016.

1036 Nowlan, C. R., Liu, X., Janz, S. J., Kowalewski, M. G., Chance, K., Follette-Cook, M. B., Fried, A., González  
1037 Abad, G., Herman, J. R., Judd, L. M., Kwon, H. A., Loughner, C. P., Pickering, K. E., Richter, D., Spinei, E.,  
1038 Walega, J., Weibring, P., and Weinheimer, A. J.: Nitrogen dioxide and formaldehyde measurements from the  
1039 GEOstationary Coastal and Air Pollution Events (GEO-CAPE) Airborne Simulator over Houston, Texas, Atmos.  
1040 Meas. Tech., 11, 5941-5964, <https://doi.org/10.5194/amt-11-5941-2018>, 2018.

1041 Oetjen, H., Baidar, S., Krotkov, N. A., Lamsal, L. N., Lechner, M., and Volkamer, R.: Airborne MAX-DOAS  
1042 measurements over California: Testing the NASA OMI tropospheric NO<sub>2</sub> product, J. Geophys. Res.-Atmos., 118,  
1043 7400-7413, <https://doi.org/10.1002/jgrd.50550>, 2013.

1044 Peng, J., Hu, M., Guo, S., Du, Z., Zheng, J., Shang, D., Zamora, M. L., Zeng, L., Shao, M., and Wu, Y.-S.:  
1045 Markedly enhanced absorption and direct radiative forcing of black carbon under polluted urban environments,  
1046 Proc. Natl. Acad. Sci. U.S.A., 201602310, <https://doi.org/10.1073/pnas.1602310113>, 2016.

1047 Peters, E., Wittrock, F., Großmann, K., Frieß, U., Richter, A., and Burrows, J. P.: Formaldehyde and nitrogen  
1048 dioxide over the remote western Pacific Ocean: SCIAMACHY and GOME-2 validation using ship-based MAX-  
1049 DOAS observations, Atmos. Chem. Phys., 12, 11179-11197, <https://doi.org/10.5194/acp-12-11179-2012>, 2012.

1050 Reddy, B. S. K., Kumar, K. R., Balakrishnaiah, G., Gopal, K. R., Reddy, R. R., Sivakumar, V., Lingaswamy, A.  
1051 P., Arafath, S. M., Umadevi, K., and Kumari, S. P.: Analysis of diurnal and seasonal behavior of surface ozone  
1052 and its precursors (NO<sub>x</sub>) at a semi-arid rural site in Southern India, Aerosol Air Qual Res, 12, 1081-1094,  
1053 <https://doi.org/10.4209/aaqr.2012.03.0055> 2012.

1054 Reed, A. J., Thompson, A. M., Kollonige, D. E., Martins, D. K., Tzortziou, M. A., Herman, J. R., Berkoff, T. A.,  
1055 Abuhassan, N. K., and Cede, A.: Effects of local meteorology and aerosols on ozone and nitrogen dioxide  
1056 retrievals from OMI and pandora spectrometers in Maryland, USA during DISCOVER-AQ 2011, Journal of  
1057 atmospheric chemistry, 72, 455-482, <https://doi.org/10.1007/s10874-013-9254-9>, 2015.

1058 Reed, C., Evans, M. J., Carlo, P. D., Lee, J. D., and Carpenter, L. J.: Interferences in photolytic NO<sub>2</sub>  
1059 measurements: explanation for an apparent missing oxidant?, Atmos. Chem. Phys., 16, 4707-4724,  
1060 <https://doi.org/10.5194/acp-16-4707-2016>, 2016.

1061 Richter, A., Begoin, M., Hilboll, A., and Burrows, J. P.: An improved NO<sub>2</sub> retrieval for the GOME-2 satellite  
1062 instrument, Atmos. Meas. Tech., 4, 1147-1159, <https://doi.org/10.5194/amt-4-1147-2011>, 2011.

1063 Russell, A. R., Valin, L. C., and Cohen, R. C.: Trends in OMI NO<sub>2</sub> observations over the United States: effects of  
1064 emission control technology and the economic recession, Atmos. Chem. Phys., 12, 12197-12209,  
1065 <https://doi.org/10.5194/acp-12-12197-2012>, 2012.

1066 Saha, S., Moorthi, S., Wu, X., Wang, J., Nadiga, S., Tripp, P., Behringer, D., Hou, Y. T., Chuang, H.-y., and  
1067 Iredell, M.: NCEP climate forecast system version 2 (CFSv2) 6-hourly products, available at  
1068 <https://rda.ucar.edu/datasets/ds094.0/>, <https://doi.org/10.5065/D61C1TXF>, 2011 (last access: Mar 10, 2015).



1069 Sawamura, P., Müller, D., Hoff, R. M., Hostetler, C. A., Ferrare, R. A., Hair, J. W., Rogers, R. R., Anderson, B.  
1070 E., Ziemba, L. D., and Beyersdorf, A. J.: Aerosol optical and microphysical retrievals from a hybrid  
1071 multiwavelength lidar data set–DISCOVER-AQ 2011, *Atmos. Meas. Tech.*, 7, 3095-3112,  
1072 <https://doi.org/10.5194/amt-7-3095-2014>, 2014.

1073 Seinfeld, J. H., and Pandis, S. N.: *Atmospheric chemistry and physics: from air pollution to climate change*, John  
1074 Wiley & Sons, Inc, Hoboken, New Jersey, 2016.

1075 Sen, B., Toon, G. C., Osterman, G. B., Blavier, J.-F., Margitan, J. J., Salawitch, R. J., and Yue, G. K.:  
1076 Measurements of reactive nitrogen in the stratosphere, *J. Geophys. Res.-Atmos.*, 103, 3571-3585,  
1077 <https://doi.org/10.1029/97JD02468>, 1998.

1078 Shin, H. H., and Hong, S.-Y.: Intercomparison of planetary boundary-layer parametrizations in the WRF model  
1079 for a single day from CASES-99, *Boundary-Layer Meteorology*, 139, 261-281, [https://doi.org/10.1007/s10546-](https://doi.org/10.1007/s10546-010-9583-z)  
1080 [010-9583-z](https://doi.org/10.1007/s10546-010-9583-z), 2011.

1081 Silvern, R. F., Jacob, D. J., Mickley, L. J., Sulprizio, M. P., Travis, K. R., Marais, E. A., Cohen, R. C., Laughner,  
1082 J. L., Choi, S., Joiner, J., and Lamsal, L. N.: Using satellite observations of tropospheric NO<sub>2</sub> columns to infer  
1083 long-term trends in US NO<sub>x</sub> emissions: the importance of accounting for the free tropospheric NO<sub>2</sub> background,  
1084 *Atmos. Chem. Phys.*, 19, 8863-8878, <https://doi.org/10.5194/acp-19-8863-2019>, 2019.

1085 Souri, A. H., Choi, Y., Jeon, W., Li, X., Pan, S., Diao, L., and Westenbarger, D. A.: Constraining NO<sub>x</sub> emissions  
1086 using satellite NO<sub>2</sub> measurements during 2013 DISCOVER-AQ Texas campaign, *Atmos. Environ.*, 131, 371-  
1087 381, <https://doi.org/10.1016/j.atmosenv.2016.02.020>, 2016.

1088 Souri, A. H., Choi, Y., Pan, S., Curci, G., Nowlan, C. R., Janz, S. J., Kowalewski, M. G., Liu, J., Herman, J. R.,  
1089 and Weinheimer, A. J.: First top - down estimates of anthropogenic NO<sub>x</sub> emissions using high - resolution  
1090 airborne remote sensing observations, *J. Geophys. Res.-Atmos.*, 123, 3269-3284,  
1091 <https://doi.org/10.1002/2017JD028009>, 2018.

1092 Spinei, E., Cede, A., Swartz, W. H., Herman, J., and Mount, G. H.: The use of NO<sub>2</sub> absorption cross section  
1093 temperature sensitivity to derive NO<sub>2</sub> profile temperature and stratospheric–tropospheric column partitioning  
1094 from visible direct-sun DOAS measurements, *Atmos. Meas. Tech.*, 7, 4299-4316, [https://doi.org/10.5194/amt-7-](https://doi.org/10.5194/amt-7-4299-2014)  
1095 [4299-2014](https://doi.org/10.5194/amt-7-4299-2014), 2014.

1096 Spurr, R.: LIDORT and VLIDORT: Linearized pseudo-spherical scalar and vector discrete ordinate radiative  
1097 transfer models for use in remote sensing retrieval problems, in: *Light Scattering Reviews 3*, Springer, 229-275,  
1098 2008.

1099 Thompson, A. M., Stauffer, R. M., Boyle, T. P., Kollonige, D. E., Miyazaki, K., Tzortziou, M., Herman, J. R.,  
1100 Abuhassan, N., Jordan, C. E., and Lamb, B. T.: Comparison of Near - Surface NO<sub>2</sub> Pollution With Pandora Total  
1101 Column NO<sub>2</sub> During the Korea - United States Ocean Color (KORUS OC) Campaign, *J. Geophys. Res.-Atmos.*,  
1102 124, 13560-13575, <https://doi.org/10.1029/2019JD030765>, 2019.

1103 Thornton, J. A., Wooldridge, P. J., and Cohen, R. C.: Atmospheric NO<sub>2</sub>: In situ laser-induced fluorescence  
1104 detection at parts per trillion mixing ratios, *Anal. Chem.*, 72, 528-539, <https://doi.org/10.1021/ac9908905>, 2000.

1105 Tong, D., Lamsal, L., Pan, L., Ding, C., Kim, H., Lee, P., Chai, T., Pickering, K. E., and Stajner, I.: Long-term  
1106 NO<sub>x</sub> trends over large cities in the United States during the great recession: Comparison of satellite retrievals,  
1107 ground observations, and emission inventories, *Atmos. Environ.*, 107, 70-84,  
1108 <https://doi.org/10.1016/j.atmosenv.2015.01.035>, 2015.

1109 Travis, K. R., Jacob, D. J., Fisher, J. A., Kim, P. S., Marais, E. A., Zhu, L., Yu, K., Miller, C. C., Yantosca, R.  
1110 M., and Sulprizio, M. P.: Why do models overestimate surface ozone in the Southeast United States?, *Atmos.*  
1111 *Chem. Phys.*, 16, 13561-13577, <https://doi.org/10.5194/acp-16-13561-2016>, 2016.

1112 Tu, J., Xia, Z.-G., Wang, H., and Li, W.: Temporal variations in surface ozone and its precursors and  
1113 meteorological effects at an urban site in China, *Atmospheric Research*, 85, 310-337,  
1114 <https://doi.org/10.1016/j.atmosres.2007.02.003>, 2007.

1115 Valin, L. C., Russell, A. R., Hudman, R. C., and Cohen, R. C.: Effects of model resolution on the interpretation  
1116 of satellite NO<sub>2</sub> observations, *Atmos. Chem. Phys.*, 11, 11647-11655, [https://doi.org/10.5194/acp-11-11647-](https://doi.org/10.5194/acp-11-11647-2011)  
1117 [2011](https://doi.org/10.5194/acp-11-11647-2011), 2011.

1118 van der A, R. J., Eskes, H. J., Roozendael, M. V., De Smedt, I., Blond, N., Boersma, F., Weiss, A., and van Peet,  
1119 J. C. A.: Algorithm Document Tropospheric NO<sub>2</sub>, available at [http://www.temis.nl/docs/AD\\_NO2.pdf1.0](http://www.temis.nl/docs/AD_NO2.pdf1.0), 23,  
1120 2010.

1121 Van Geffen, J., Boersma, K., Van Roozendael, M., Hendrick, F., Mahieu, E., De Smedt, I., Sneepe, M., and  
1122 Veefkind, J.: Improved spectral fitting of nitrogen dioxide from OMI in the 405–465 nm window, *Atmos. Meas.*  
1123 *Tech.*, 8, 1685-1699, <https://doi.org/10.5194/amt-8-1685-2015>, 2015.

1124 Van Stratum, B. J. H., Vilà-Guerau de Arellano, J., Ouwersloot, H. G., Dries, K. d., Van Laar, T. W., Martinez,  
1125 M., Lelieveld, J., Diesch, J.-M., Drewnick, F., and Fischer, H.: Case study of the diurnal variability of chemically  
1126 active species with respect to boundary layer dynamics during DOMINO, *Atmos. Chem. Phys.*, 12, 5329-5341,  
1127 <https://doi.org/10.5194/acp-12-5329-2012>, 2012.

1128 Wooldridge, P. J., Perring, A. E., Bertram, T. H., Flocke, F. M., Roberts, J. M., Singh, H. B., Huey, L. G.,  
1129 Thornton, J. A., Wolfe, G. M., and Murphy, J. G.: Total Peroxy Nitrates ([Sigma] PNs) in the atmosphere: the  
1130 Thermal Dissociation-Laser Induced Fluorescence (TD-LIF) technique and comparisons to speciated PAN  
1131 measurements, *Atmos. Meas. Tech.*, 3, 593, <https://doi.org/10.5194/amt-3-593-2010>, 2010.

1132 Yuan, H., McGinley, J. A., Schultz, P. J., Anderson, C. J., and Lu, C.: Short-range precipitation forecasts from  
1133 time-lagged multimodel ensembles during the HMT-West-2006 campaign, *Journal of Hydrometeorology*, 9, 477-  
1134 491, <https://doi.org/10.1175/2007JHM879.1>, 2008.

1135 Zhang, R., Wang, Y., Smeltzer, C., Qu, H., Koshak, W., and Boersma, K. F.: Comparing OMI-based and EPA  
1136 AQS in situ NO<sub>2</sub> trends: towards understanding surface NO<sub>x</sub> emission changes, *Atmos. Meas. Tech.*, 11, 3955-  
1137 3967, <https://doi.org/10.5194/amt-11-3955-2018>, 2018.

1138 Zhang, Y., and Wang, Y.: Climate-driven ground-level ozone extreme in the fall over the Southeast United  
1139 States, *Proc. Natl. Acad. Sci. U.S.A.*, 113, 10025-10030, <https://doi.org/10.1073/pnas.1602563113>, 2016.

1140 Zhang, Y., Wang, Y., Chen, G., Smeltzer, C., Crawford, J., Olson, J., Szykman, J., Weinheimer, A. J., Knapp, D.  
1141 J., and Montzka, D. D.: Large vertical gradient of reactive nitrogen oxides in the boundary layer: Modeling  
1142 analysis of DISCOVER - AQ 2011 observations, *J. Geophys. Res.-Atmos.*, 121, 1922-1934,  
1143 <https://doi.org/10.1002/2015JD024203>, 2016.

1144 Zhao, C., Wang, Y., Choi, Y., and Zeng, T.: Summertime impact of convective transport and lightning NO<sub>x</sub>  
1145 production over North America: modeling dependence on meteorological simulations, *Atmos. Chem. Phys.*, 9,  
1146 4315-4327, <https://doi.org/10.5194/acp-9-4315-2009>, 2009.

1147 Zhao, X., Griffin, D., Fioletov, V., McLinden, C., Davies, J., Ogyu, A., Lee, S. C., Lupu, A., Moran, M. D.,  
1148 Cede, A., Tiefengraber, M., and Müller, M.: Retrieval of total column and surface NO<sub>2</sub> from Pandora zenith-sky  
1149 measurements, *Atmos. Chem. Phys.*, 19, 10619-10642, <https://doi.org/10.5194/acp-19-10619-2019>, 2019.

1150 Zhao, X., Griffin, D., Fioletov, V., McLinden, C., Cede, A., Tiefengraber, M., Müller, M., Bognar, K., Strong,  
1151 K., Boersma, F., Eskes, H., Davies, J., Ogyu, A., and Lee, S. C.: Assessment of the quality of TROPOMI high-  
1152 spatial-resolution NO<sub>2</sub> data products in the Greater Toronto Area, *Atmos. Meas. Tech.*, 13, 2131-2159,  
1153 <https://doi.org/10.5194/amt-13-2131-2020>, 2020.

1154 Zheng, Y., Alapaty, K., Herwehe, J. A., Del Genio, A. D., and Niyogi, D.: Improving high-resolution weather  
1155 forecasts using the Weather Research and Forecasting (WRF) Model with an updated Kain–Fritsch scheme,  
1156 *Monthly Weather Review*, 144, 833-860, <https://doi.org/10.1175/MWR-D-15-0005.1>, 2016.

1157



**Table 1.** Comparison of the concentrations of NO<sub>y</sub> and its components between REAM and P-3B aircraft measurements during the DISCOVER-AQ campaign

		NO <sub>y</sub> / ppb <sup>1</sup>	NO / ppb	NO <sub>2</sub> _NCAR / ppb	NO <sub>2</sub> _LIF / ppb <sup>2</sup>	ΣPNs / ppb	ΣANs / ppb	HNO <sub>3</sub> / ppb	Derived-NO <sub>y</sub> / ppb <sup>3</sup>
36-km <sup>4</sup>	Weekday <sup>5</sup>	P-3B	2.51 ± 2.09	0.18 ± 0.29	0.85 ± 1.13	0.68 ± 0.95	0.31 ± 0.23	1.15 ± 0.73	2.86 ± 2.26
		REAM	3.64 ± 3.13	0.18 ± 0.30	0.74 ± 1.04	0.68 ± 0.89	0.10 ± 0.09	1.80 ± 1.61	3.10 ± 2.70
		R <sup>2</sup>	0.33	0.35	0.38	0.34	0.38	0.24	0.41
	Weekend	P-3B	3.00 ± 2.18	0.15 ± 0.20	0.71 ± 0.80	0.63 ± 0.72	0.91 ± 0.53	1.15 ± 0.79	2.96 ± 2.15
4-km		REAM	3.78 ± 2.20	0.15 ± 0.17	0.54 ± 0.59	0.53 ± 0.58	0.09 ± 0.06	2.31 ± 1.38	3.43 ± 2.26
		R <sup>2</sup>	0.29	0.28	0.41	0.45	0.27	0.50	0.51
	Weekday	P-3B	2.51 ± 2.15	0.19 ± 0.30	0.86 ± 1.27	0.68 ± 0.98	0.70 ± 0.59	1.17 ± 0.74	2.90 ± 2.27
		REAM	3.81 ± 3.81	0.19 ± 0.35	0.79 ± 1.31	0.76 ± 1.20	0.46 ± 0.51	2.03 ± 1.91	3.31 ± 3.28
		R <sup>2</sup>	0.28	0.22	0.26	0.32	0.37	0.38	0.47
	Weekend	P-3B	2.96 ± 2.13	0.14 ± 0.18	0.69 ± 0.74	0.63 ± 0.71	0.91 ± 0.51	1.15 ± 0.80	2.94 ± 2.09
		REAM	4.36 ± 3.66	0.25 ± 0.40	0.85 ± 1.28	0.81 ± 1.23	0.41 ± 0.29	2.54 ± 1.99	3.72 ± 3.52
		R <sup>2</sup>	0.21	0.15	0.19	0.18	0.16	0.23	0.37

<sup>1</sup> For P-3B, the concentrations of NO<sub>y</sub>, NO, and NO<sub>2</sub>\_NCAR were measured by using the NCAR 4-channel chemiluminescence instrument. The measurement uncertainties are 10%, 10 - 15%, and 10% for NO, NO<sub>2</sub>, and NO<sub>y</sub>, respectively. The 1-second, 1-sigma detection limits are 20 pptv, 30 pptv, and 20 pptv for NO, NO<sub>2</sub>, and NO<sub>y</sub>, respectively ([https://discover-aq.larc.nasa.gov/pdf/2010STM/Weinheimer20101005\\_DISCOVERAQ\\_AJW.pdf](https://discover-aq.larc.nasa.gov/pdf/2010STM/Weinheimer20101005_DISCOVERAQ_AJW.pdf)). For REAM, NO<sub>y</sub> is the sum of NO, NO<sub>2</sub>, total peroxyacyl nitrates (ΣPNs), total alkyl nitrates (ΣANs) (include alkyl nitrates and hydroxyalkyl nitrates), HNO<sub>3</sub>, HONO, 2 × N<sub>2</sub>O<sub>5</sub>, HNO<sub>4</sub>, first generation C5 carbonyl nitrate (nighttime isoprene nitrate ISN1: C<sub>5</sub>H<sub>8</sub>NO<sub>4</sub>), 2 × C5 dihydroxydinitrate (DHDN: C<sub>5</sub>H<sub>10</sub>O<sub>8</sub>N<sub>2</sub>), methyl peroxy nitrate (MPN: CH<sub>3</sub>O<sub>2</sub>NO<sub>2</sub>), propanone nitrate (PROPNN: CH<sub>3</sub>C(=O)CH<sub>2</sub>ONO<sub>2</sub>), nitrate from methyl vinyl ketone (MVKN: HOCH<sub>2</sub>CH(ONO<sub>2</sub>)C(=O)CH<sub>3</sub>), nitrate from methacrolein (MARCN: HOCH<sub>2</sub>C(ONO<sub>2</sub>)(CH<sub>3</sub>)CHO), and ethanol nitrate (ETHLN: CHOCH<sub>2</sub>ONO<sub>2</sub>).

<sup>2</sup> For P-3B, the concentrations of NO<sub>2</sub>\_LIF, ΣPNs, ΣANs, and HNO<sub>3</sub> were measured by applying the thermal dissociation-laser induced fluorescence (TD-LIF) technique. The accuracy of TD-LIF measurements from TD-LIF measurements with those from REAM, we calculate derived-NO<sub>y</sub> as the sum of NO, NO<sub>2</sub>\_LIF, ΣPNs, ΣANs, and HNO<sub>3</sub> is ~ 10 ppt 10 s<sup>-1</sup> (Day et al., 2002).

<sup>3</sup> To compare NO<sub>y</sub> concentrations from TD-LIF measurements of all the five species are available at the same hour in the same grid cell, we can calculate derived-NO<sub>y</sub> at the given hour in the given grid cell. Therefore, in Table 1, the averaged derived-NO<sub>y</sub> values are not exactly equal to the sum of averaged NO, NO<sub>2</sub>\_LIF, ΣPNs, ΣANs, and HNO<sub>3</sub> concentrations that only depend on the availability of a single species. In addition, the measurement times and frequencies between NO<sub>y</sub> and derived-NO<sub>y</sub> are not the same. A comparison between these two types of data needs coincident sampling, as described in the main text.

<sup>4</sup> Mean NO<sub>x</sub> emissions over the six P-3B spiral sites are close (relative difference < 4%) between the 36-km and 4-km REAM (Table S1).

<sup>5</sup> Due to different sampling times and locations between weekdays and weekends, we do not recommend a direct comparison between weekday and weekend values here.

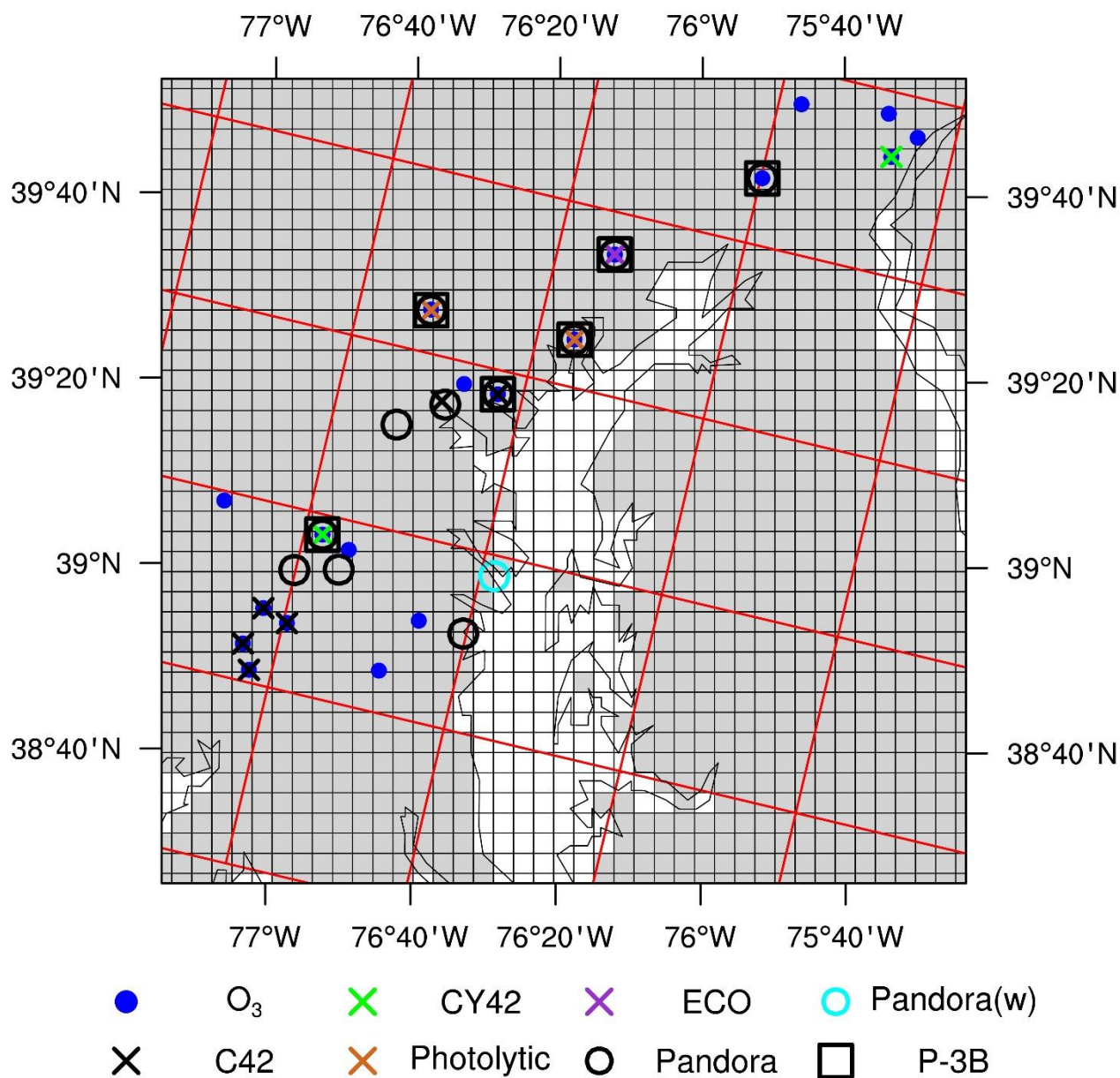


**Figure 1.** The locations of surface and P-3B aircraft observations during the DISCOVER-AQ 2011 campaign. We mark the 36-km REAM grid cells with red lines and the 4-km REAM grid cells with black lines. Gray shading denotes land surface in the nested 4-km WRF domain, while white area denotes ocean/water surface. Blue dots denote surface  $O_3$  observation sites. Cross-marks denote surface  $NO_2$  observation sites, and their colors denote different measurement instruments: green for the Thermo Electron 42C-Y  $NO_y$  analyzer, dark orchid for the Ecotech Model 9841/9843 T- $NO_y$  analyzers, black for the Thermo Model 42C  $NO_x$  analyzer, and chocolate for the Teledyne API model 200eup photolytic  $NO_x$  analyzer. Circles denote Pandora sites, and the cyan circle denotes a Pandora site (USNA) on a ship. Black squares denote the inland P-3B aircraft spiral locations.

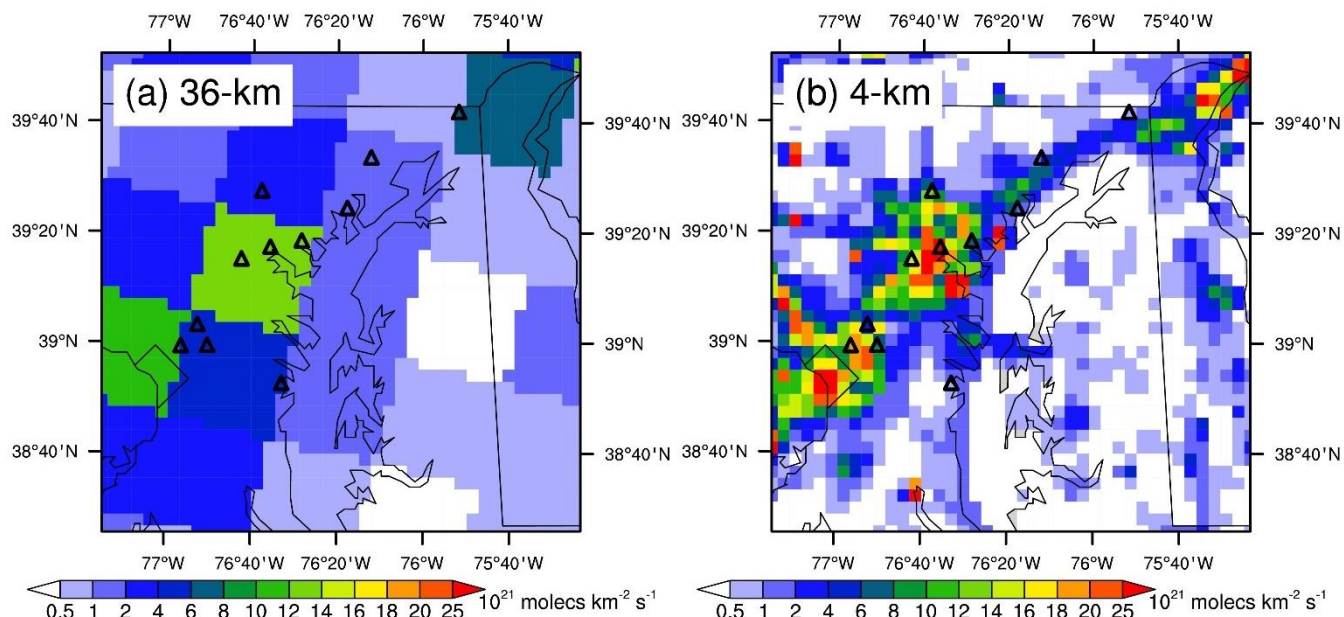


**Figure 2.** Distributions of NO<sub>x</sub> emissions for the (a) 36-km and (b) 4-km REAM simulations around the DISCOVER-AQ 2011 region. Here NO<sub>x</sub> emissions refer to the mean values (molecules km<sup>-2</sup> s<sup>-1</sup>) in one week (Monday – Sunday).

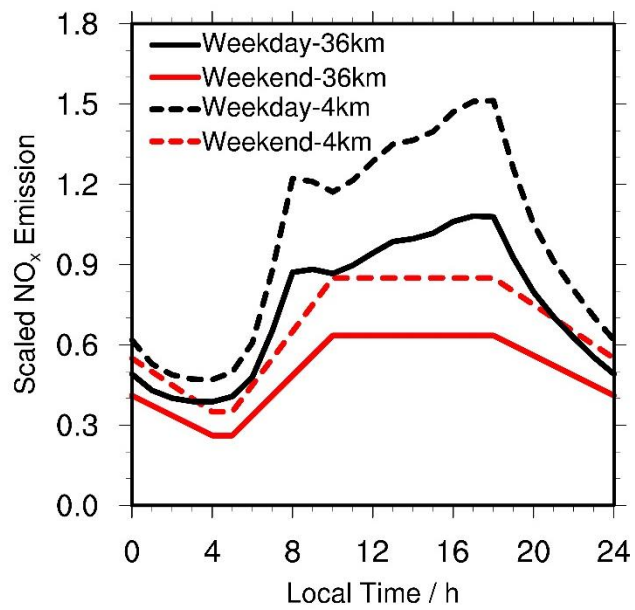


**Figure 3.** Relative diurnal profiles of weekday and weekend NO<sub>x</sub> emissions (molecules km<sup>-2</sup> s<sup>-1</sup>) in the DISCOVER-AQ 2011 region (the 36/4 km grid cells over the 11 inland Pandora sites shown in Figure 1) for the 36-km and 4-km REAM. All the profiles are scaled by the 4-km weekday emission average value (molecules km<sup>-2</sup> s<sup>-1</sup>).

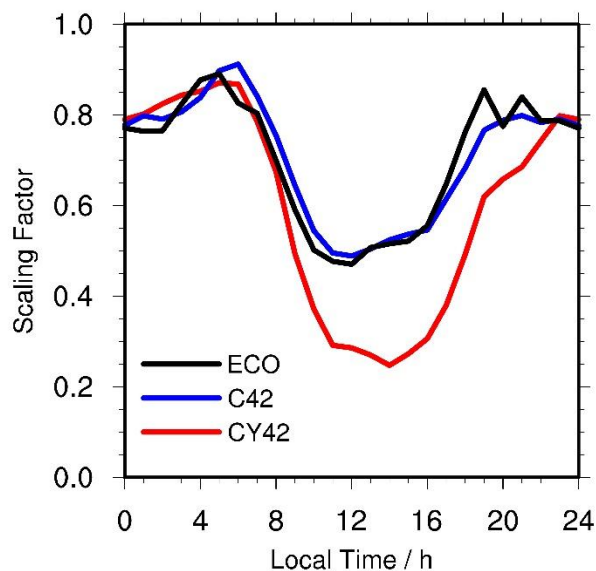


**Figure 4.** Hourly ratios of NO<sub>2</sub> measurements from the Teledyne API model 200 eup photolytic NO<sub>x</sub> analyzer to NO<sub>2</sub> from coincident catalytic instruments for 2011 July. “CY42” denotes the ratios of photolytic NO<sub>2</sub> to NO<sub>2</sub> from the Thermo Electron 42C-Y NO<sub>y</sub> analyzer in Edgewood, “C42” denotes the ratios of photolytic NO<sub>2</sub> to NO<sub>2</sub> from the Thermo Model 42C NO<sub>x</sub> analyzer in Padonia, and “ECO” denotes the ratios of photolytic NO<sub>2</sub> to NO<sub>2</sub> from the Ecotech Model 9841 T-NO<sub>y</sub> analyzer in Padonia. “ECO” ratios are also used to scale NO<sub>2</sub> measurements from the Ecotech Model 9843 T-NO<sub>y</sub> analyzer.

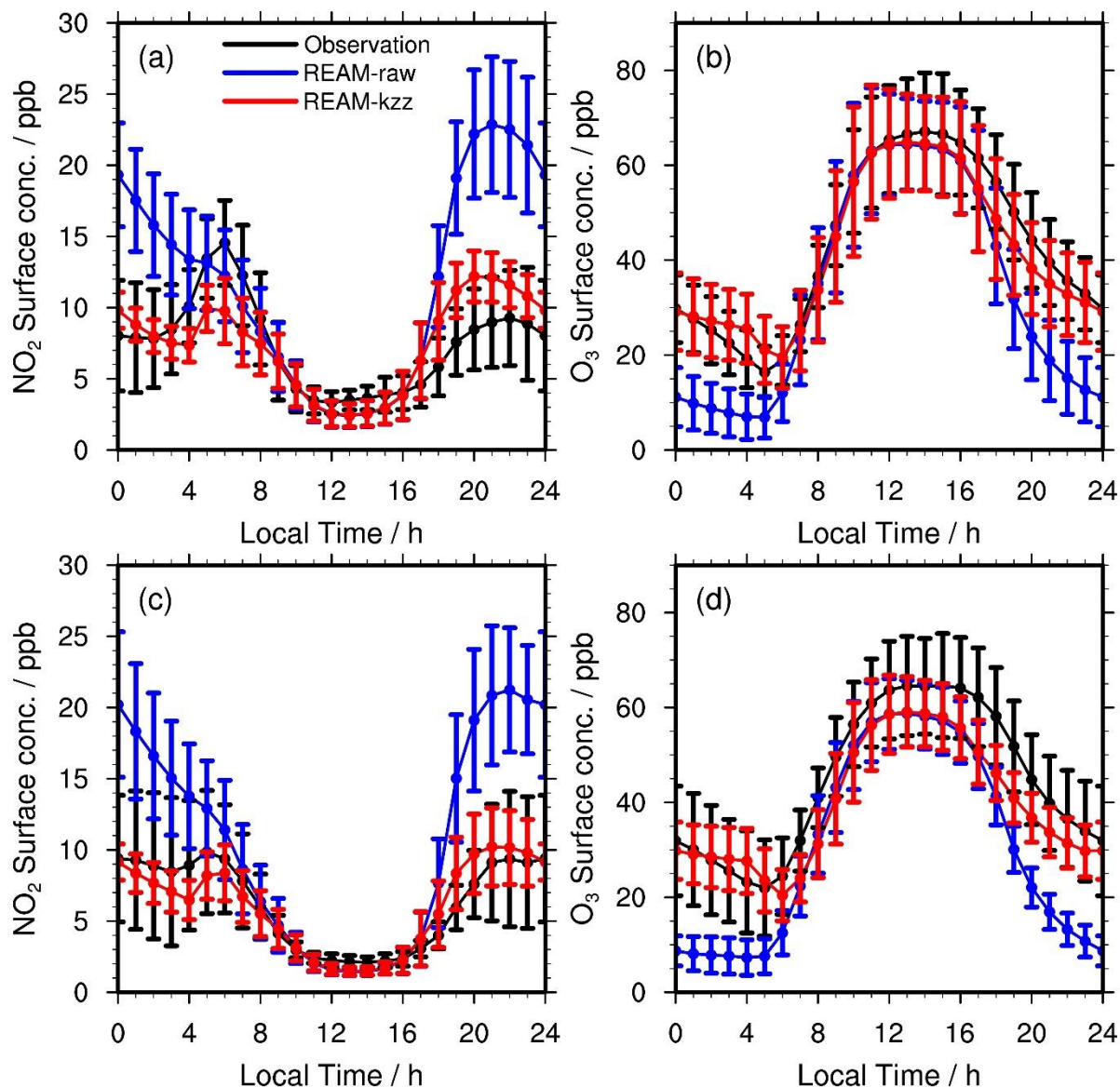


**Figure 5.** Diurnal cycles of surface (a, c)  $\text{NO}_2$  and (b, d)  $\text{O}_3$  concentrations on (a, b) weekdays and (c, d) weekends during the DISCOVER-AQ campaign in the DISCOVER-AQ region (the 36-km grid cells over the 11 inland Pandora sites shown in Figure 1). Black lines denote the mean observations from all the 11  $\text{NO}_2$  surface monitoring sites and 19  $\text{O}_3$  surface sites during the campaign (Figure 1), as mentioned in Section 2.5. “REAM-raw” (blue lines) denotes the coincident 36-km REAM simulation results with WRF-YSU simulated  $k_{zz}$  data, and “REAM-kzz” (red lines) is the coincident 36-km REAM simulation results with updated  $k_{zz}$  data. See the main text for details. Vertical bars denote corresponding standard deviations.

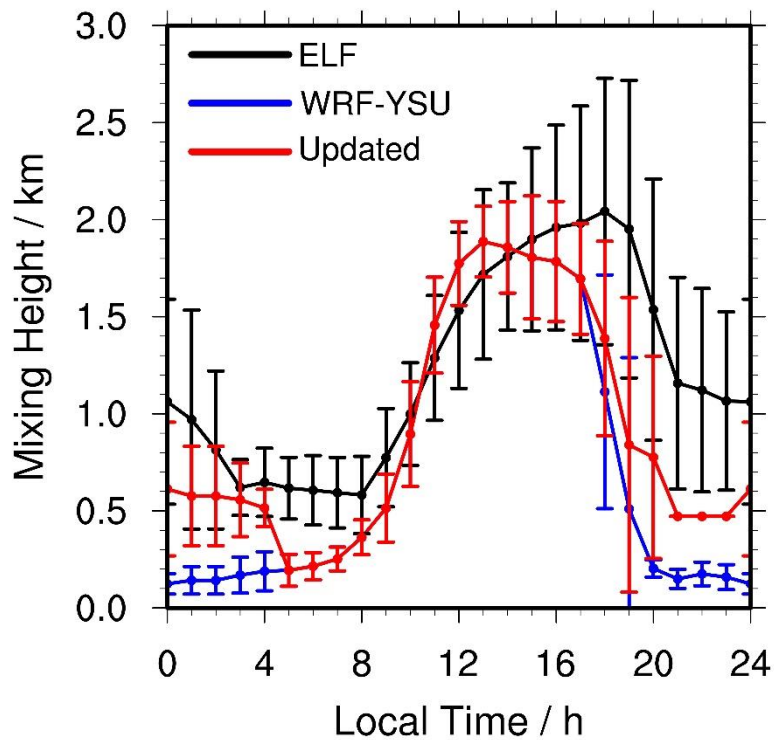


**Figure 6.** ELF observed and model simulated diurnal variations of PBLH at the UMBC site during the Discover-AQ campaign. “ELF” denotes ELF derived PBLHs by using the covariance wavelet transform method. “WRF-YSU” denotes the 36-km WRF-YSU  $k_{zz}$ -determined PBLHs, and “Updated” denotes updated  $k_{zz}$ -determined PBLHs. See the main text for details. Vertical bars denote standard deviations.



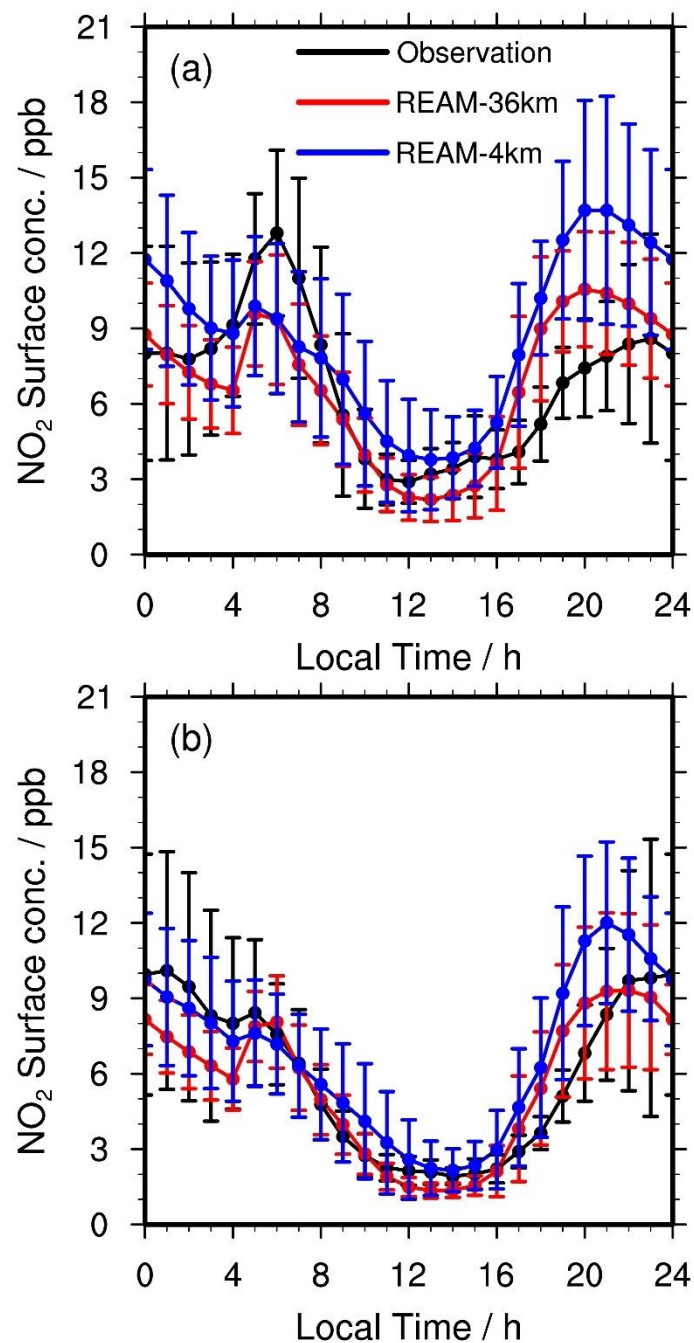
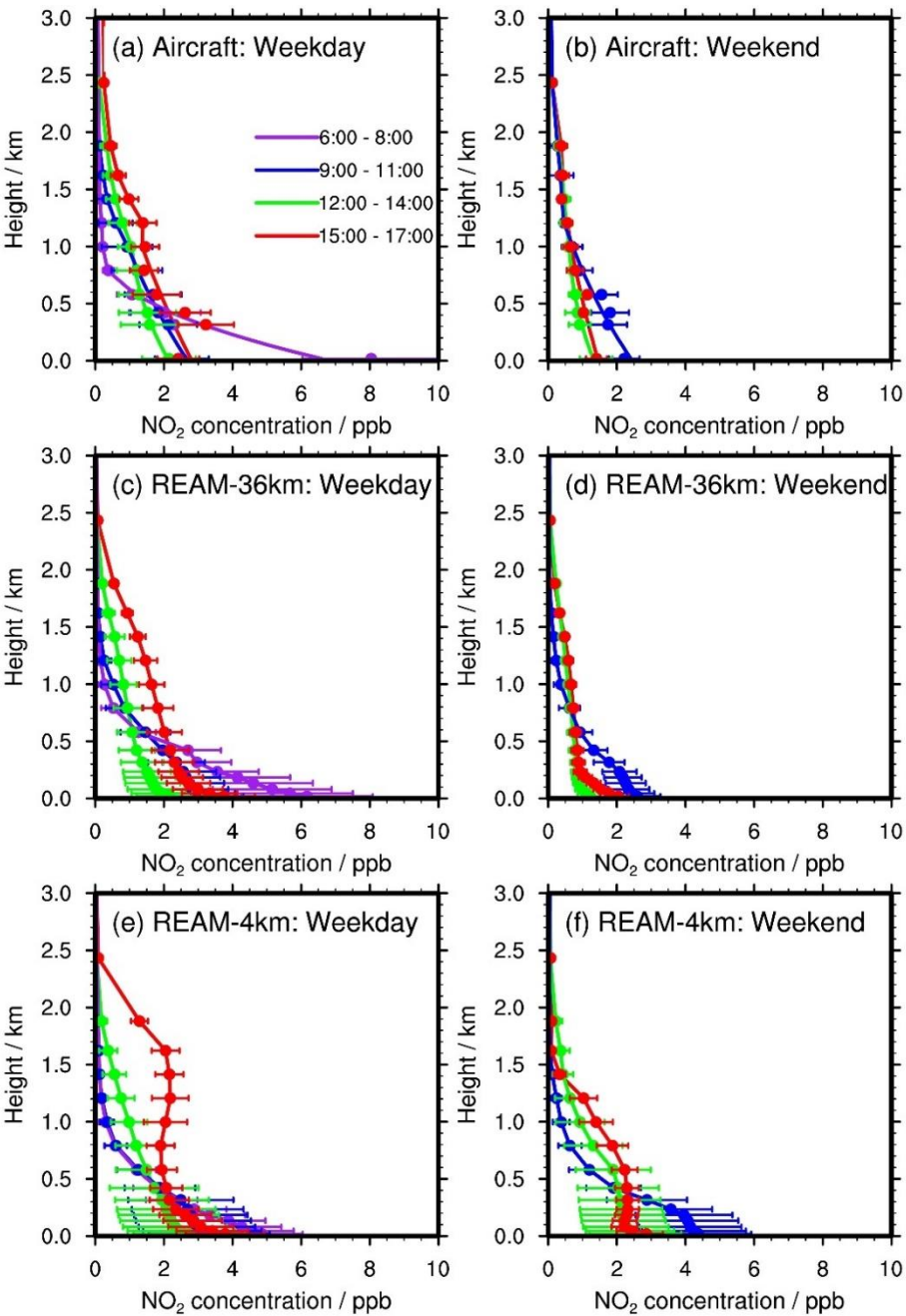


**Figure 7.** Diurnal cycles of observed and simulated average surface  $\text{NO}_2$  concentrations over Padonia, Oldtown, Essex, Edgewood, Beltsville, and Aldino (Table S1) on (a) weekdays and (b) weekends. Black lines denote mean observations from the six sites. Red lines denote coincident 36-km REAM simulation results, and blue lines are for coincident 4-km REAM simulation results. Error bars denote standard deviations.





1225 **Figure 8.** Temporal evolutions of NO<sub>2</sub> vertical profiles below 3 km on (a, c, e) weekdays and (b, d, f) weekends from the (a,  
1226 b) P-3B aircraft and (c, d) 36-km and (e, f) 4-km REAM during the DISCOVER-AQ campaign. Horizontal bars denote the  
1227 corresponding standard deviations. In (a) and (b), dots denote aircraft measurements, while lines below 1 km are based on  
1228 quadratic polynomial fitting, as described in section 2.6. The fitting values are mostly in reasonable agreement with the  
1229 aircraft and surface measurements in the boundary layer. On weekends, no aircraft observations were made at 6:00 – 8:00  
1230 LT, and therefore no corresponding model profiles are shown.  
1231

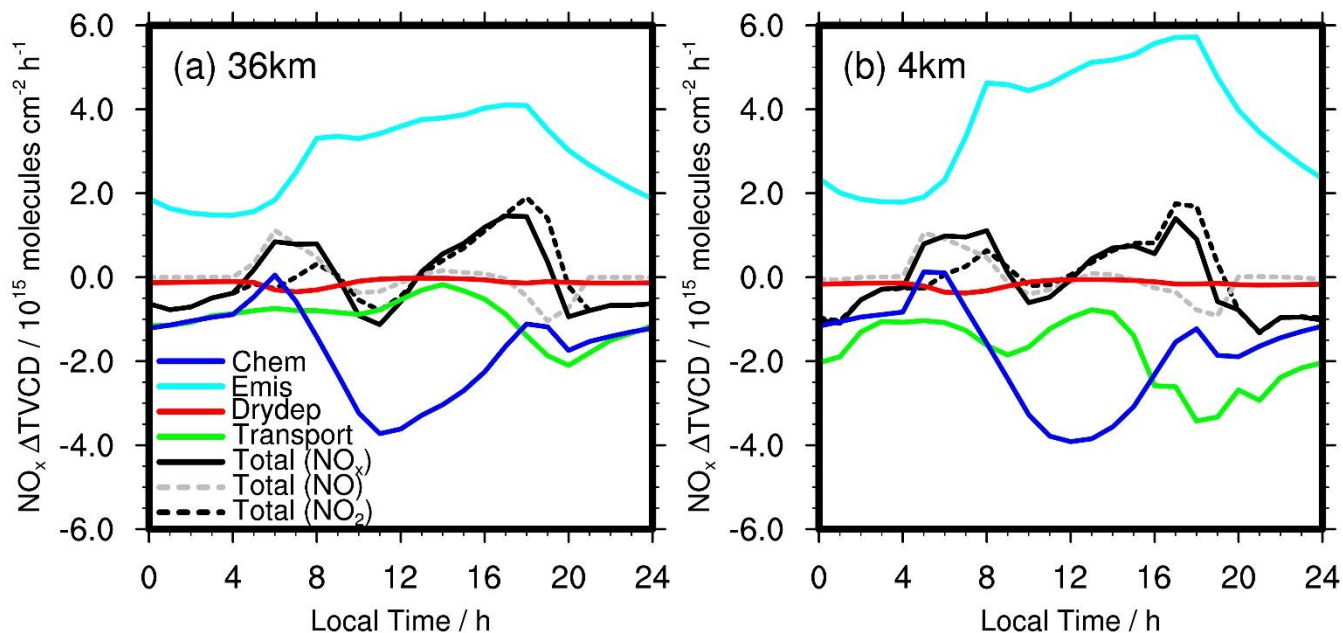


**Figure 9.** Contributions of emission, chemistry, transport, and dry deposition to  $\text{NO}_x$  TVCD diurnal variations over the 11 inland Pandora sites (Table S1 and Figure 1) on weekdays in July 2011 for the (a) 36-km and (b) 4-km REAM simulations. “Chem” refers to net  $\text{NO}_x$  chemistry production; “Emis” refers to  $\text{NO}_x$  emissions; “Drydep” denotes  $\text{NO}_x$  dry depositions; “Transport” includes advection, turbulent mixing, lightning  $\text{NO}_x$  production, and wet deposition. “Total ( $\text{NO}_x$ )” is the hourly change of  $\text{NO}_x$  TVCDs ( $\Delta(\text{TVCD}) = \text{TVCD}_{t+1} - \text{TVCD}_t$ ). “Total ( $\text{NO}_2$ )” is the hourly change of  $\text{NO}_2$  TVCDs, and “Total ( $\text{NO}$ )” is the hourly change of  $\text{NO}$  TVCDs.

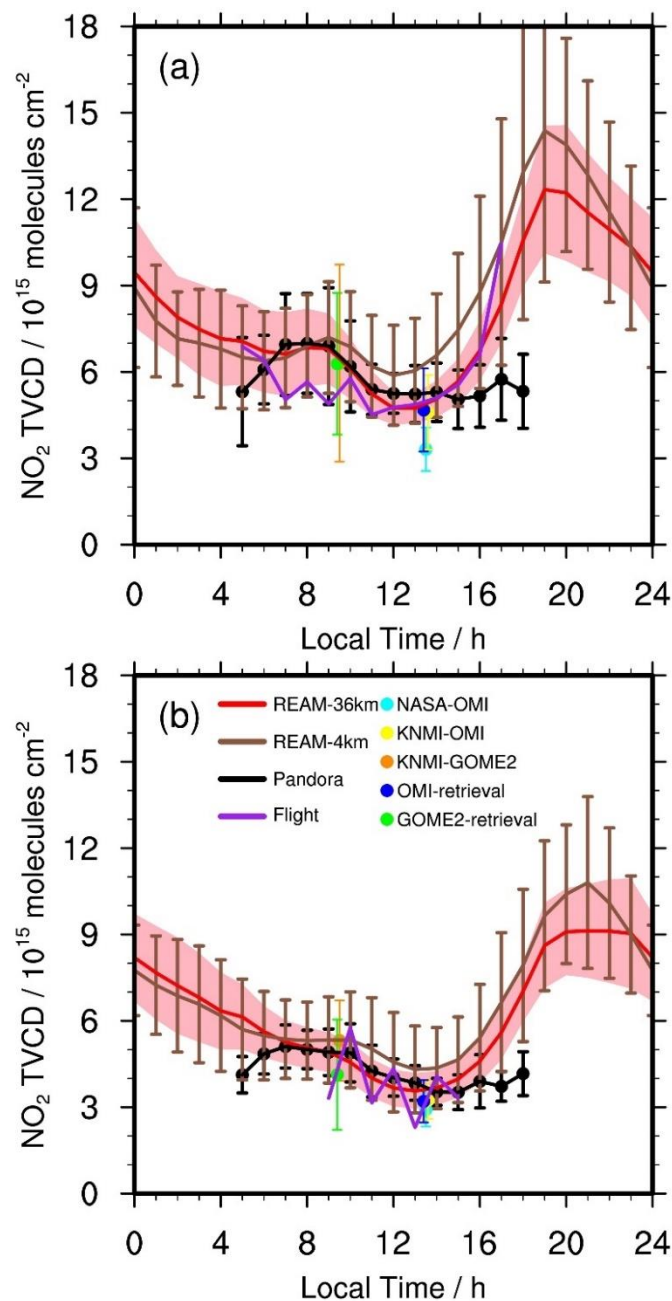
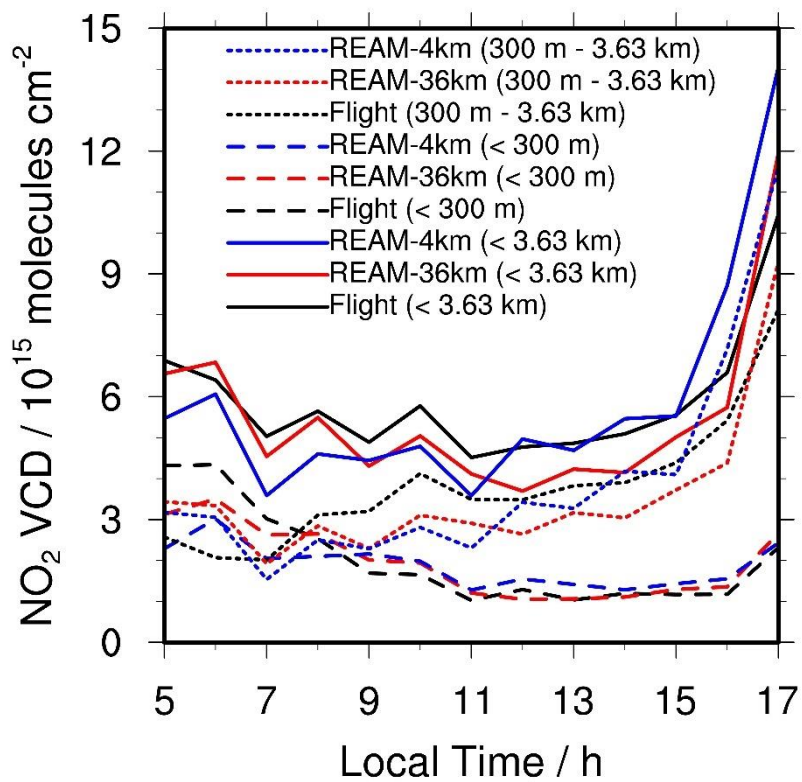


**Figure 10.** Daily variations of NO<sub>2</sub> TVCDs on (a) weekdays and (b) weekends during the DISCOVER-AQ campaign. “REAM-36km” refers to the 36-km REAM simulation results over the 11 inland Pandora sites. “REAM-4km” refers to the 4-km REAM simulation results over the 11 inland Pandora sites. “Pandora” refers to updated Pandora TVCD data. “Flight” denotes P-3B aircraft-derived NO<sub>2</sub> VCDs below 3.63 km. “NASA-OMI” denotes the OMI NO<sub>2</sub> TVCDs retrieved by NASA over the Pandora sites; “KNMI-OMI” denotes the OMI NO<sub>2</sub> TVCDs from KNMI; “KNMI-GOME2” is the GOME-2A NO<sub>2</sub> TVCDs from KNMI. “OMI-retrieval” and “GOME2-retrieval” denote OMI and GOME-2A TVCDs retrieved by using the KNMI DOMINO algorithm with corresponding 36-km REAM vertical profiles, respectively. We list NO<sub>2</sub> TVCD values at 9:30 and 13:30 LT in Table S3.



1250  
1251 **Figure 11.** Weekday hourly variations of NO<sub>2</sub> VCDs at different height (AGL) bins (< 3.63 km AGL, < 300 m AGL, and  
1252 300 m ~ 3.63 km AGL) based on P-3B aircraft-derived datasets and the 36-km and 4-km REAM results. “Flight” denotes P-  
1253 3B aircraft-derived NO<sub>2</sub> VCDs, “REAM-36km” denotes coincident 36-km REAM simulated VCDs, and “REAM-4km”  
1254 denotes coincident 4-km REAM simulated VCDs.  
1255

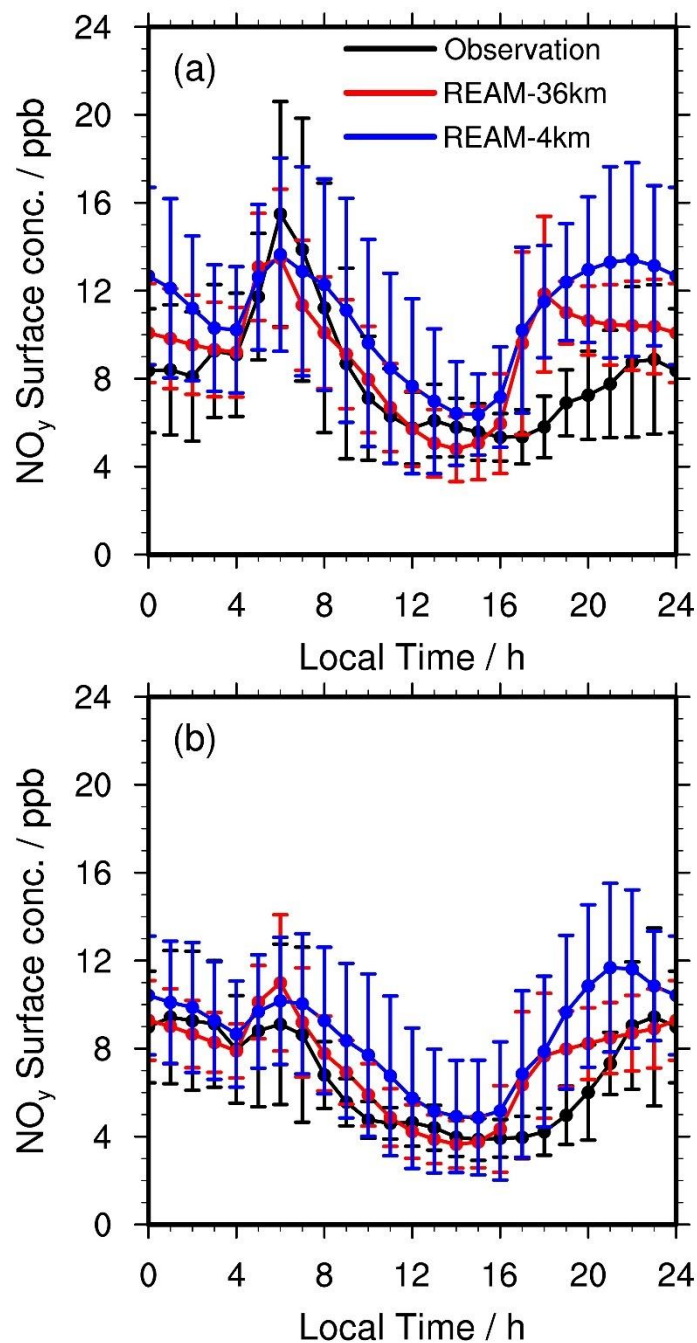


**Figure 12.** Diurnal cycles of observed and simulated average surface  $\text{NO}_y$  concentrations at Padonia, Edgewood, Beltsville, and Aldino on (a) weekdays and (b) weekends. Vertical bars denote the corresponding standard deviations. It is noteworthy that the mean  $\text{NO}_x$  emissions over Padonia, Edgewood, Beltsville, and Aldino are 99% higher in the 4-km than the 36-km REAM simulations (Table S1).

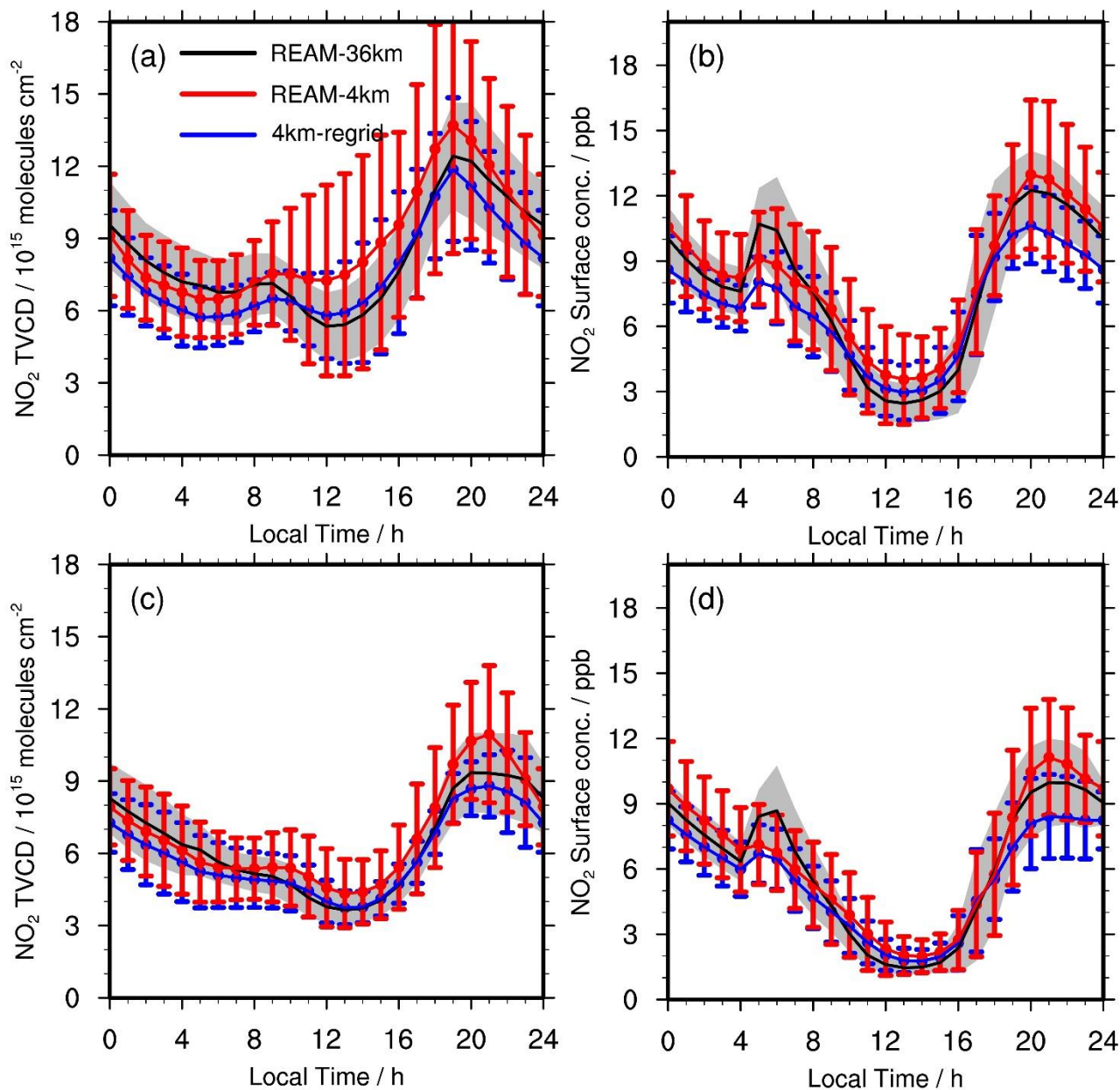


**Figure 13.** Comparisons of NO<sub>2</sub> (a, c) TVCDs and (b, d) surface concentrations over the 11 inland Pandora sites between the 4-km and 36-km REAM simulations on (a, b) weekdays and (c, d) weekends for July 2011. “REAM-36km” (black lines) denotes the 36-km REAM simulation results; “REAM-4km” (red lines) denotes the 4-km REAM simulation results; “4km-regrid” (blue lines) refers to the 36-km values by re-gridding the 4-km REAM simulation results into 36-km REAM grid cells. Error bars denote standard deviations.



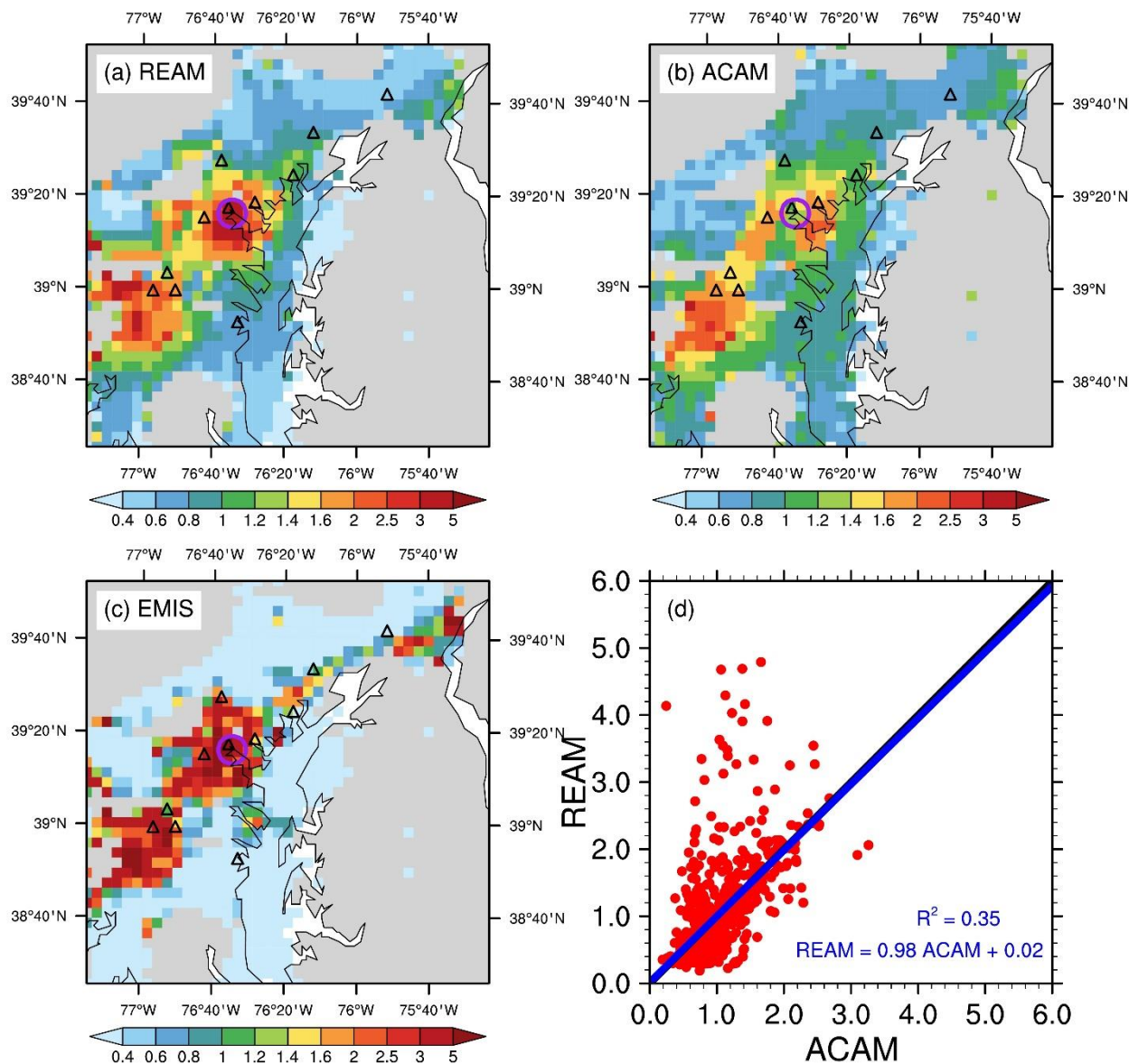


**Figure 14.** Distributions of the scaled mean (a) ACAM NO<sub>2</sub> VCDs below the UC-12 aircraft and (b) coincident 4-km REAM simulation results on weekdays in July 2011. (c), the distribution of the scaled NEI2011 NO<sub>x</sub> emissions on weekdays. The purple circles denote a small region surrounded by high-NO<sub>x</sub> emission pixels and with high NO<sub>2</sub> VCDs in the 4-km REAM but low NO<sub>2</sub> VCDs in ACAM. (d) is the scatter plot of the scaled ACAM and 4-km REAM NO<sub>2</sub> VCDs from (a) and (b). Here, we scale all values (VCDs and NO<sub>x</sub> emissions) based on their corresponding domain averages. The domain averages of ACAM and coincident 4-km REAM NO<sub>2</sub> VCDs are  $4.7 \pm 2.0$  and  $4.6 \pm 3.2 \times 10^{15}$  molecules cm<sup>-2</sup>, respectively.

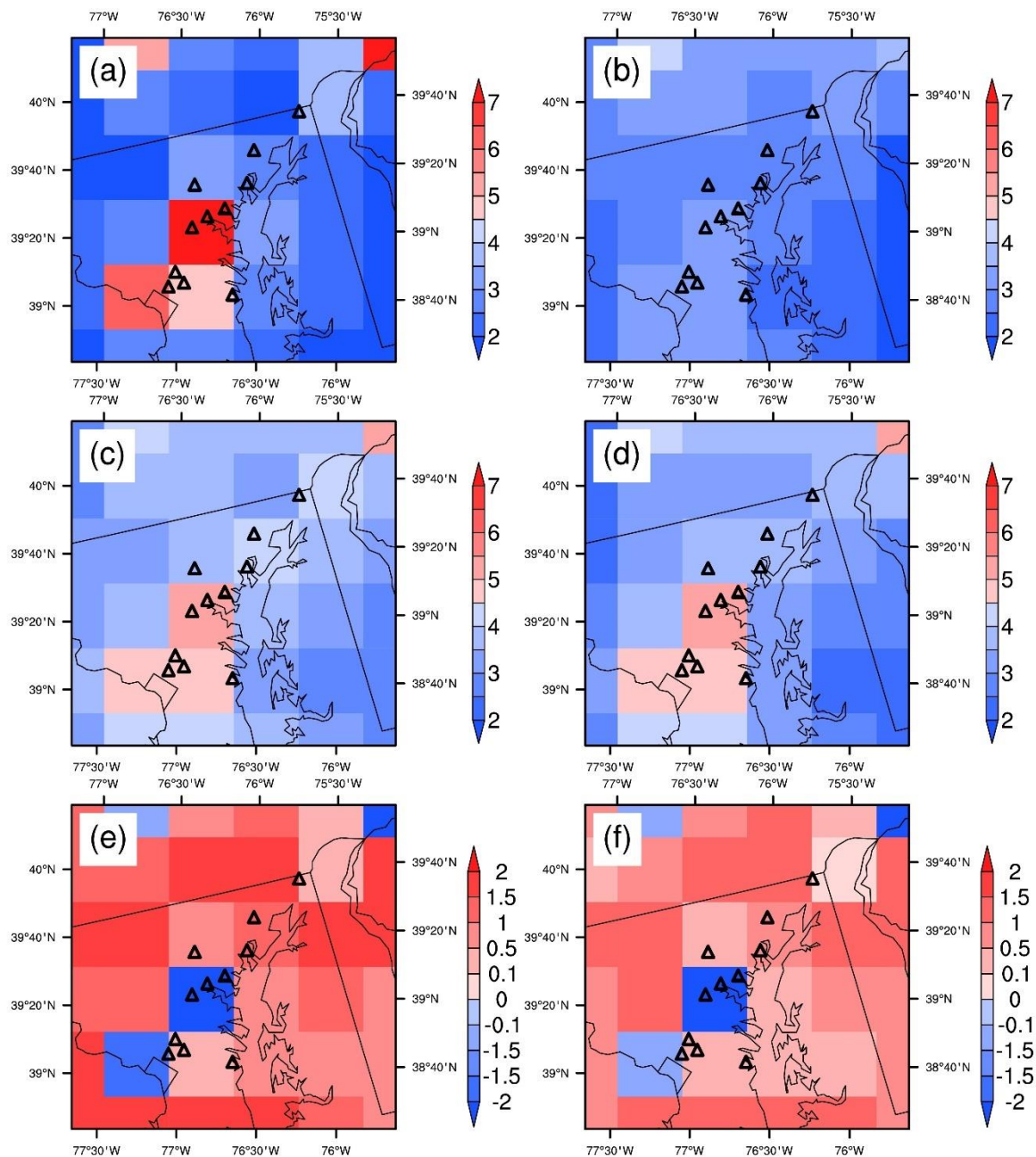


**Figure 15.** Distributions of weekday NO<sub>2</sub> TVCDs around the DISCOVER-AQ 2011 region for 13:30 LT in July 2011: (a) the 36-km REAM simulation results, (b) the NASA OMI product (OMNO2), (c) the KNMI OMI product, (d) the retrieved OMI NO<sub>2</sub> TVCDs by using the KNMI DOMINO algorithm with corresponding 36-km REAM vertical profiles, (e) the distribution of the NO<sub>2</sub> TVCD differences (c minus a) between KNMI OMI and 36-km REAM, and (f) the difference (d minus a) between retrieved OMI NO<sub>2</sub> TVCDs and the 36-km REAM results. The NO<sub>2</sub> TVCD unit is  $10^{15}$  molecules  $\text{cm}^{-2}$ .